THE ASTROPHYSICAL JOURNAL, 467:597–621, 1996 August 20

UNDERSTANDING THE KILOPARSEC-SCALE STRUCTURE OF M87

GEOFFREY V. BICKNELL[1,2] AND MITCHELL C. BEGELMAN[2,3]
Received 1995 September 21; accepted 1996 March 5

ABSTRACT

Motivated by the determination of proper motions in the M87 jet by Biretta, Zhou, & Owen, we have investigated the relationship between the dynamics of the jet in M87 and the kiloparsec-scale radio and optical structure. Our results show that relativistic effects play an important role in the appearance of shocks in relativistic jets. We argue that knot A in the M87 jet, which appears to be almost transverse to the flow, is in fact a highly oblique shock, and that the direction of its normal with respect to the flow is within about 10° of the Mach angle (the angle beyond which no shock is possible). A modest pressure jump $\lesssim 5$ at knot A is consistent with the observed small jet deflection for bulk Lorentz factors of the order of 3–5. We suggest that helical modes of the Kelvin-Helmholtz instability are responsible for the development of oblique shocks in the jet, provided that the medium external to the jet is no more than about 10–100 times denser than the jet. This implies that the kiloparsec-scale radio lobes are much less dense than the interstellar medium in the central regions of the M87 cooling flow. The radio jets in M87 are therefore driving high-pressure, low-density bubbles into the surrounding ISM. We show that the radii of the lobes are consistent with this interpretation and the inferred energy flux in the jet if the age of the inner lobes is $\sim 10^6$ yr, in agreement with that estimated by Turland. The resultant expansion of the lobes can comfortably power the excitation of the surrounding optical filaments via radiative shocks. The initial conical expansion of the M87 jet may be due to mass injection by stars along its trajectory and the thermal density of the gas within the radio lobes may be the result of a combination of mass loss from stars over the $\sim 10^6$ yr lifetime of this region of the radio source and the sweeping up of clouds that have condensed out of the interstellar medium. Since the knots in the M87 jet appear to be regions of transient overpressure inside an overpressured bubble, it is not necessary to invoke magnetic confinement of the jet. The fact that the inner lobes of M87 appear to be comparatively young regions immersed in a much larger and older structure, evident at low frequency, suggests that the output from the black hole in M87 fluctuates on a timescale of 10^6–10^7 yr. Intermittency may result from the ejected radio plasma "choking off" the mass accretion into the nucleus via the cooling flow.

Subject headings: galaxies: individual (M87) — galaxies: jets — galaxies: structure — shock waves

1. INTRODUCTION

The "curious straight ray" discovered by Curtis (1918) in the galaxy M87 has occupied a central role in the study of active galaxies ever since it was identified with the strong radio source Virgo A (Bolton, Stanley, & Slee 1949). M87 contains one of the closest examples of an extragalactic jet and has therefore been observed at very high spatial resolution. It is the only jet in which relativistic proper motion has been measured definitively on kiloparsec scales (Biretta, Zhou, & Owen 1995). Moreover, spectra of the jet and its environs have been obtained over wavelengths ranging from radio through infrared, optical, and ultraviolet to X-ray. The proximity of M87, the fact that it has been observed in so many spectral bands, and the proposition that the physics of relativistic flow is important for understanding many of the properties of radio-loud active galaxies means that it is extremely important to understand this source in detail. However, to date, a comprehensive theory of the M87 jet and the associated kiloparsec-scale radio source has been lacking. In this paper, therefore, we propose a theory which attempts to unify the properties of the jet, the kiloparsec-scale radio source and the optical line-emitting filaments surrounding it.

In outline, our theory is as follows: M87 is a twin jet source in which each jet is relativistic with a Lorentz factor $\gtrsim 3$, and the approaching jet is observed at an angle $\sim 30°$–$35°$ with respect to the line of sight. Over the last $\sim 10^6$ yr the jets have produced bubbles in the local interstellar medium (ISM) that are contaminated by thermal material from stellar mass loss. As each jet propagates through its corresponding bubble, it becomes unstable as a result of helical ($m = 1$) Kelvin-Helmholtz modes which result in oblique shocks as the supersonic flow adjusts to the continual changes in jet direction. The system of oblique shocks gives rise to the impression that filaments are wound around the jet (Owen, Hardee, & Cornwell 1989) and also dictates the appearance of most of the knots in the jet. We suggest that the brightest knot (knot A), which appears to be almost transverse to the jet, is in fact oblique, and that its appearance is due to a combination of viewing angle and relativistic effects. The shocks increase in strength as the amplitude of the instability grows, until they become so strong that they disrupt the jet, near knot C. The shocks propagate at the group velocity of the instability, and this is consistent with the observed knot proper motions, for the range of parameters indicated in § 4. (Note that this velocity is considerably slower than the bulk flow speed of the jet.) We suggest that the steep spectral break in each knot (with a change in spectral index $\Delta\alpha > 0.5$) is due to the cooling of

[1] Australian National University Astrophysical Theory Centre. The ANUATC is operated jointly by the Mount Stromlo and Siding Spring Observatories and the School of Mathematical Sciences of the Australian National University; geoff@mso.anu.edu.au.

[2] JILA, University of Colorado, Boulder, CO 80309-0440; mitch@jila.colorado.edu.

[3] Also at Department of Astrophysical, Planetary, and Atmospheric Sciences, University of Colorado, Boulder.

postshock electrons in an inhomogeneous magnetic field, although a detailed model of this process remains to be calculated. The continual growth of the jet-fed bubble drives a shock into the surrounding ISM, and as this wave intercepts surrounding dense gas, it excites optical line emission through radiative shocks.

In the following section we summarize the pertinent observational data on M87. In succeeding sections (§ 3–7) we develop the elements of this theory. We assume a distance to M87 of 17 Mpc (Freedman et al. 1994), implying a scale of 82 pc arcsec^{-1}.

2. SUMMARY OF THE OBSERVATIONS

The observational data on the M87 jet are extensive, and the reader is referred to papers by Biretta & Meisenheimer (1993), Biretta (1993), Biretta, Stern, & Harris (1991), and Biretta et al. (1995) for detailed summaries, discussions of the observations, and an introduction to the literature. In this section we restrict ourselves to the features of the observations which are pertinent to the following sections.

2.1. *VLA and HST Images of the Jet and Knots*

The most recent and detailed VLA image of the M87 jet is the 0.″1 ≈ 8.2 pc resolution image of Biretta et al. (1995) (see also Biretta 1993). This image clearly shows almost constant cone-angle expansion of the jet out to knot A, the jet knots, the instability of the jet—most obvious from knot A outward—and the subsequent merging of the jet into the northwest radio lobe. This image also clearly shows the meandering subrelativistic portion of the proposed counterjet in the southeast lobe, beginning from near where Sparks et al. (1992) discovered the counterfeature to knot H. The projected magnetic field in the jet is parallel to the jet except at knots A and C, where it is approximately perpendicular. This is consistent with our assumption that the knots are oblique shocks. (See § 3.)

At first sight the *HST* images (see Biretta & Meisenheimer 1993) and the radio images seem identical. The similarity of the optical and radio images can be quantified by the radio-to-optical spectral index, $\alpha_{RO} = -(\log F_R - \log F_O)/(\log \nu_R - \log \nu_O)$, which shows only minor variation ($\Delta\alpha \sim 0.1$–0.2) throughout the jet. However, taking the logarithm of the ratio of the radio and optical flux densities and dividing by the long frequency baseline [$\log(\nu_R/\nu_O) \approx 6$] tends to diminish variations in the relative radio and optical fluxes. An image of the *ratio* of the optical and radio fluxes (J. A. Biretta 1994, private communication) shows larger variations (~2). Moreover, the transverse profiles of the *HST* and VLA images are quite different (Biretta 1993): the optical image is more centrally concentrated. The latter feature also argues against the jet brightness being related to shearing processes at its edge.

The ratio of the surface brightness of the M87 jet to that of the presumed counterjet is greater than 150 in the radio and greater than 450 in the optical (Biretta 1993). However, the flatter radio spectral index means that the radio observations provide the most stringent constraint on the jet velocity and viewing angle. The constraints on the jet Lorentz factor, γ, and the angle to the line of sight are shown in Figure 1 for various values of the surface brightness ratio. While it should be borne in mind that the Lorentz factor and jet direction are likely to vary from point to point, it is clear from this diagram that angles to the line of sight $\lesssim 38°$ and Lorentz factors $\gtrsim 1.5$ are essential. If the surface brightness constraints are to be comfortably satisfied, then $\theta \lesssim 35°$ and $\gamma \gtrsim 2$ are required.

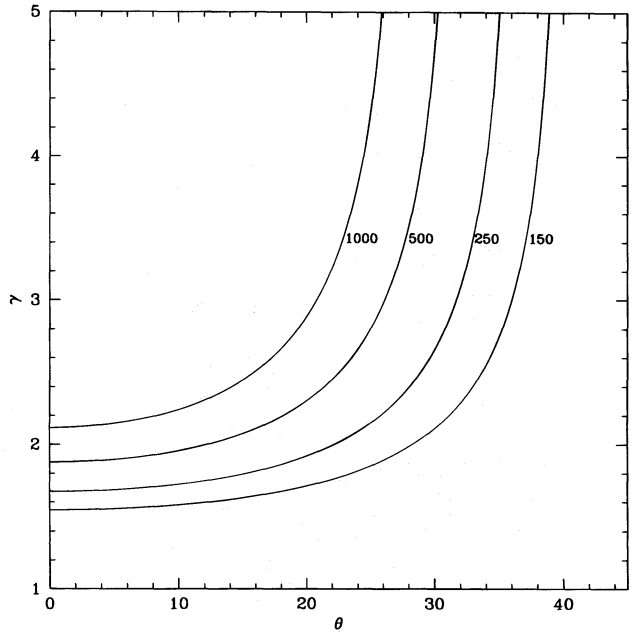

FIG. 1.—Relationship between Lorentz factor and viewing angle for various indicated values of the jet-counterjet surface brightness ratio.

2.2. *Knot Spectra*

The spectral index in the radio is $\alpha_{RR} \approx 0.5$, while the radio-to-optical spectral index of $\alpha_{RO} \approx 0.53$–0.56 reflects a gradual steepening of the spectrum from the radio to the near-infrared. The spectra of knots A, B, and D (and presumably those of the other knots) steepen considerably at approximately $10^{14.5}$ Hz, with an optical–to–X-ray spectral index $\alpha_{OX} \approx 1.5$ (Biretta et al. 1991). Furthermore, the optical spectral index, α_{OO}, steepens between knots (with ~1″ resolution) (Biretta & Meisenheimer 1993), so that there is evidence for interknot cooling of the highest energy electrons. The variation of α_{OO} at 0.″1 resolution will be of great interest, since this will tell us whether there is particle acceleration between the knots.

The low frequency to high frequency spectral break, $\Delta\alpha \sim 1$, is larger than predicted by a simple injection-plus-cooling model, for which $\Delta\alpha = 0.5$. We consider a possible explanation for this in § 5.

2.3. *Proper Motions*

Using six epochs of 15 GHz VLA data, Biretta et al. (1995) have derived proper motions of the order of 0.5 c throughout the jet, with a subfeature in knot D showing a proper motion ~2.5c. Some of the individual knot proper motions are, for knot A, $0.51 \pm 0.015\ c$; knot B, $0.62 \pm 0.05\ c$; knot C, $0.11 \pm 0.04\ c$. These authors convincingly argue that it is improbable that all of the knots have the same speed and that, in particular, the slower speed of knot C is significant. Biretta et al. (1995) also report that the velocity vectors become increasingly misaligned with respect to the jet axis, with increasing distance from the core, suggesting a connection between the velocity field and morphology. We provide the theoretical basis for this in § 4.

2.4. *Conditions in the Jet and Inner Radio Lobes*

The southeast and northwest inner radio lobes are approximately 2–3 kpc in diameter and have been imaged

with high dynamic range and 0".4 resolution by Hines, Owen & Eilek (1989). These images reveal a set of complex filaments, most of which have a minimum pressure in the range (2–6) $\times 10^{-10}$ dyn cm^{-2} with a corresponding magnetic field ~ 50 μG. Two of the brighter filaments have a mimimum pressure $\sim 10^{-9}$ dyn cm^{-2} and a magnetic field ~ 100 μG. Hines et al. (1989) calculate an interfilamentary minimum pressure $\approx 4 \times 10^{-11}$ dyn cm^{-2}. The estimates of minimum pressures in the jet knots (uncorrected for relativistic effects) range from approximately 1.5×10^{-9} to 2×10^{-8} dyn cm^{-2}, depending upon whether it is assumed that the knot emission is center-filled or originates in a thin layer at the surface of the jet. The minimum pressure in knot A is 3×10^{-9} dyn cm^{-2} if its emissivity is uniform across the jet, or is $\sim 2 \times 10^{-8}$ dyn cm^{-2} if its emissivity originates in a thin layer (Owen et al. 1989; Biretta & Meisenheimer 1993). The thermal pressure in the vicinity of the radio lobe inferred from the White & Sarazin (1988) cooling flow models is approximately (5–10) $\times 10^{-10}$ dyn cm^{-2}. Thus, the knots are overpressured with respect to the neighboring interstellar medium, and there is some indication from the brighter filaments that the lobe is also overpressured.

2.5. *The Rotation Measure*

Owen, Eilek, & Keel (1990) , using multifrequency data, have detected a large rotation measure screen illuminated by the radio source. The rotation measure, typically ~ 1000 rad m^{-2}, is mostly positive. Some regions have values ~ 8000 rad m^{-2}. Owen et al. (1990) argue that the Faraday screen envelops the lobe in a thick boundary layer and that the magnetic field in the layer ~ 20–40 μG.

2.6. *The Hot Atmosphere of M87*

M87 has long been known to be surrounded by a hot ($T \approx 2 \times 10^7$ K) atmosphere, observations of which have been used to constrain the distribution of mass in M87 at large radii. However, it is the distribution of gas in the inner few kiloparsecs that is of main concern here. The central regions are quite dense, with a central electron density $n_e \approx 0.2$ cm^{-3} and a pressure that varies from $p \approx 2 \times 10^{-9}$ to $p \approx 3 \times 10^{-10}$ dyn cm^{-2} over the extent of the inner radio lobes (White & Sarazin 1988). This small variation is consistent with the size of the optical core radius, $r_c \approx 790$ pc (Sargent et al. 1978).

Böhringer et al. (1995) have published *ROSAT* observations of M87 which show interesting deficits and enhancements of X-ray emission in the vicinity of, but exterior to, the inner radio lobes. In particular, to the north of the northwest lobe and north of the optically emitting filaments there is a deficit of X-ray surface brightness. Böhringer et al. (1995) also present a 12" radio image which is sensitive to larger scale emission than the Hines et al. (1989) 0".4 resolution image. The Böhringer et al. (1995) data show plumes originating from the inner lobes and extending for some kiloparsecs into the surrounding medium. Enhancements of X-ray emission are correlated with parts of the plumes.

2.7. *The Optical Emission-Line Filaments*

The emission-line filaments in M87 were first studied in detail by Ford & Butcher (1979) and have subsequently been reobserved by Sparks, Ford, & Kinney (1993). Most of the filamentary structures lie outside the inner radio lobes. However, they appear to be connected to the gaseous disk (Ford et al. 1994) in the nucleus of M87. The [S II] line ratio is at the low-density limit (F. N. Owen 1995, private communication), so that the electron density satisfies $n_e \lesssim 100$ cm^{-3}. The filaments cover an effective area ≈ 1250 arcsec$^2 = 8.5 \times 10^6$ pc^2, and the Hα + N II luminosity is $\approx 3 \times 10^{40}$ ergs s^{-1}. Ford & Butcher (1979) remarked on the similarity of the spectrum to the spectra of supernova remnants for which shocks are an obvious excitation mechanism. The velocities of the filaments well outside the nucleus are typically blueshifted with respect to systemic by ~ 100 km s^{-1}, although there is one filament 12" from the nucleus which is redshifted by ≈ 150 km s^{-1} and velocities up to 430 km s^{-1} are observed. The velocity dispersion in the filaments is ~ 100–150 km s^{-1}. Sparks et al. (1993) also argued that the filaments lie in front of the radio lobes. For a complete description of the velocity field and morphology the reader should consult Figure 8 of Sparks et al. (1993).

Binette, Dopita, & Tuohy (1985) originally modeled the filaments as radiative shocks with velocities ~ 100–200 km s^{-1}, making approximate allowance for the photoionizing radiation produced by the postshock plasma. M. Dopita (1995, private communication) has recently modeled the spectrum of the circumnuclear disk of M87 using the latest version of the MAPPINGS line emission code (Sutherland & Dopita 1993), which consistently incorporates the effects of photoionizing radiation from the postshock region. The parameters of his model are a shock velocity of 200 km s^{-1} and a magnetic parameter $Bn^{-1/2} = 8$ μG cm$^{3/2}$. A reasonably strong magnetic field is required to prevent the recombining gas from becoming too dense. Similar shock parameters would also apply to the filaments, since the line ratios are very similar.

3. MORPHOLOGY, KINEMATICS, AND DYNAMICS OF KNOT A

3.1. *Time Retardation and the Appearance of Knot A*

In our opinion, the knots in the M87 jet are most naturally explained as oblique internal shocks. The appearance and inferred magnetic field structure of the knots support this proposal. Oblique shocks in relativistic jets may exhibit substantial proper compression ratios and pressure jumps without disrupting the flow. Moreover, they are readily produced in a number of circumstances. Indeed, transverse shocks tend to become unstable and evolve into oblique shocks (D. Clarke 1994, private communication). However, in the case of M87, we propose (§ 4) that the oblique shocks are triggered directly by growth of a Kelvin-Helmholtz instability, and that the jet is eventually disrupted by the train of shocks starting from knot A.

Knot A seems to violate the rule of oblique shocks: it appears to be almost transverse to the flow. However, we show here that this transverse appearance can be attributed partly to relativistic effects as well as to a fortuitous viewing direction. We model knot A as a planar surface of high emissivity that propagates down the jet at a pattern speed β_p (relative to the observer's frame). The normal to the plane need not coincide with the jet axis, as it would for a transverse shock; indeed, we argue below, on observational grounds, that it is inclined by a moderately large angle. In order to describe the *apparent* shape of the surface on the sky, we first set up an observer's coordinate system as

shown in Figure 2. This coordinate system and the mathematical details of the appearance of a relativistic shock are described in the Appendix. However, we note here two of the principal results of the Appendix. First, the observed (nonunit) shock normal, $\boldsymbol{m}$, differs from the intrinsic (unit) shock normal, $\boldsymbol{n}$, according to

$$\boldsymbol{m} = \boldsymbol{n} - \beta_n \boldsymbol{k}_{\rm obs} , \tag{3.1}$$

where $\beta_n = \beta_p \cos \psi_{\rm jet}$ is the component of the shock velocity parallel to the shock normal, $\psi_{\rm jet}$ is the angle between the intrinsic shock normal and the pattern velocity vector (assumed to lie parallel to the jet axis), and $\boldsymbol{k}_{\rm obs}$ is the unit vector in the direction of the observer. For convenience of notation in the following we refer to the components of the unit normal corresponding to $\boldsymbol{m}$ by $\hat{\boldsymbol{m}}$. Second, consistent with the apparent proper motion of a relativistically moving feature in a jet (Rees 1966), the apparent proper motion of the shock on the sky is

$$\beta_a = \frac{\beta_p \sin \theta}{1 - \beta_p \cos \theta} , \tag{3.2}$$

with the corresponding reverse transformation

$$\beta_p = \frac{\beta_a}{\sin \theta + \beta_a \cos \theta} . \tag{3.3}$$

In order for a given apparent motion to correspond to a physical speed ($\beta_p < 1$), one requires $\theta < 2 \tan^{-1} \beta_a^{-1}$.

To constrain the geometry, we note that knot A, in contrast to the other knots in the M87 jet, has unusually sharp brightness contours, particularly along the side closest to the nucleus. Moreover, its overall shape is highly elongated along a direction approximately 18° from the normal to the projected jet axis (Biretta et al. 1995). As suggested by Biretta (1993), we infer from these observations that knot A is observed nearly "edge-on," i.e., our line of sight is nearly tangent to the apparent plane of the emitting surface. This is partly the result of time retardation, which tends to favor edge-on morphologies. It is straightforward to see why this is the case from equation (A16) for the $z_{\rm obs}$ component of the observed normal,

$$m_{z,\rm obs} = -\sin \theta n_{x,\rm jet} + (\cos \theta - \beta_p) n_{z,\rm jet} . \tag{3.4}$$

In general, when relativistic effects are important for the appearance of a jet, then the angle θ is reasonably small, implying that $\sin \theta \ll 1$ and $\cos \theta \sim 1$. It follows, when $\beta_p \sim 1$, that for many viewing angles, $(\cos \theta - \beta_p) \ll 1$, implying $m_{z,\rm obs} \ll 1$. Thus, the shock normal *appears* to lie close to the plane of the sky.

The contour plots in Figure 3 illustrate this point. These contours are determined in the following way: We define polar angles $(\psi_{\rm jet}, \phi_{\rm jet})$ and $(\psi_{\rm obs}, \phi_{\rm obs})$ to describe the shock normal in the jet frame and the apparent shock normal in the observer's frame, respectively. The angle $\psi_{\rm jet}$ is defined in Figure 2, while $\phi_{\rm jet}$ is the azimuthal angle measured with respect to the plane containing the jet axis and the observer's line of sight. The angle $\phi_{\rm obs}$ defines the projected position angle of the shock normal on the sky, relative to the projected jet axis. The angle $\psi_{\rm obs}$ denotes the apparent tilt of the shock normal out of the plane of the sky, with $\psi_{\rm obs} = 90°$ corresponding to an edge-on shock. Equations (A19), (A20), (A15), and (A17) define the transformation between $(\psi_{\rm jet}, \phi_{\rm jet})$ and $(\psi_{\rm obs}, \phi_{\rm obs})$. The contours $\psi_{\rm obs}$ = constant and $\phi_{\rm obs}$ = constant are plotted in the $\psi_{\rm jet} - \phi_{\rm jet}$ plane, for various values of β_a and θ, in Figure 3.

For reference, the upper left-hand panel of Figure 3 shows the contours for a jet at an inclination of 30° when relativistic effects are not important (i.e., $\beta_a = 0$). The upper right-hand and lower left-hand panels show the contours for parameters which are relevant to knot A, e.g., $\beta_a = 0.509$ and $\theta = 25°$, 30°, respectively. The lower right-hand panel shows the situation when $\beta_a = 5$ and $\theta = 20°$, typical of the jet in a BL Lac object. The latter plot is presented here, since it clearly has relevance for the appearance of shocks in superluminal sources and is an extreme example of the effect.

These contour plots show that the contours in the vicinity of $\psi_{\rm obs} = 90°$ (apparent edge-on morphology) are expanded for larger β_a, relative to the equivalent contours for $\beta_a = 0$. This means that the shock appears almost edge-on even while the shock normal in the jet frame ranges through a large solid angle. If we constrain the observed normal to be, say, within 20% of being edge on, i.e., $-0.2 < \hat{m}_{z,\rm obs} < 0.2$ (corresponding to the normal being within approximately 10° of edge-on), then the probability of this occurring for a random distribution of normal orientations in the jet frame is approximately 0.31 when $\theta = 30°$ and $\beta_a = 0.51$. This should be compared to 0.2 for the nonrelativistic case. Thus, there is a significant increase in the probability of observing a nearly edge-on shock. Although the following point is not directly relevant to the M87 jet, this probability increases to 0.42 when $\beta_a = 5$ and $\theta = 20°$.

The left-hand panel of Figure 4 shows the functional relationship between the jet-frame polar angle $\psi_{\rm jet}$ and the

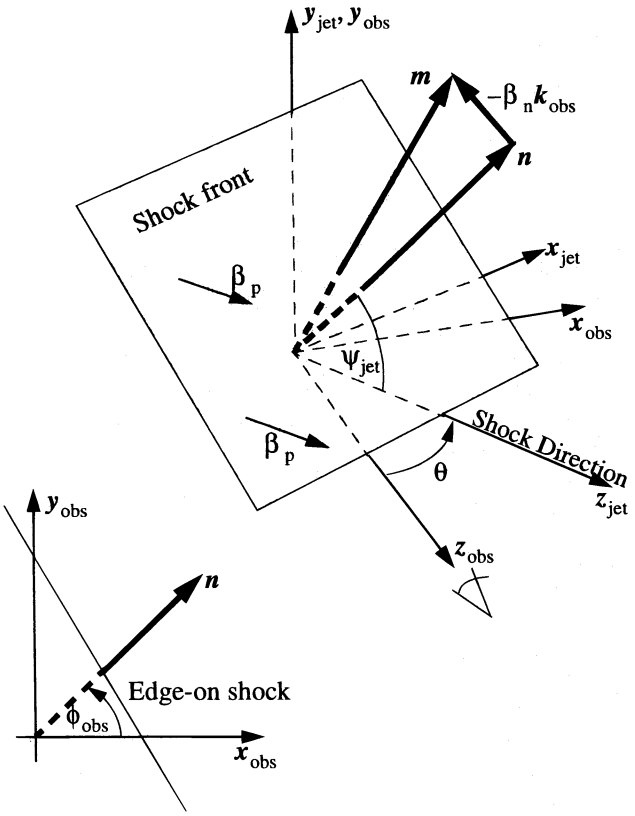

FIG. 2.—Jet and observer coordinate system used in § 3. The $z_{\rm jet}$ axis points in the direction of the shock pattern speed, and the $z_{\rm obs}$ axis points in the direction of the observer. The $x_{\rm obs}$ and $y_{\rm obs}$ axes lie in the plane of the sky. The unit vector $\boldsymbol{n}$ is the normal to the shock; $\boldsymbol{m}$ is the apparent normal. The unit vector $\boldsymbol{k}_{\rm obs}$ points toward the observer.

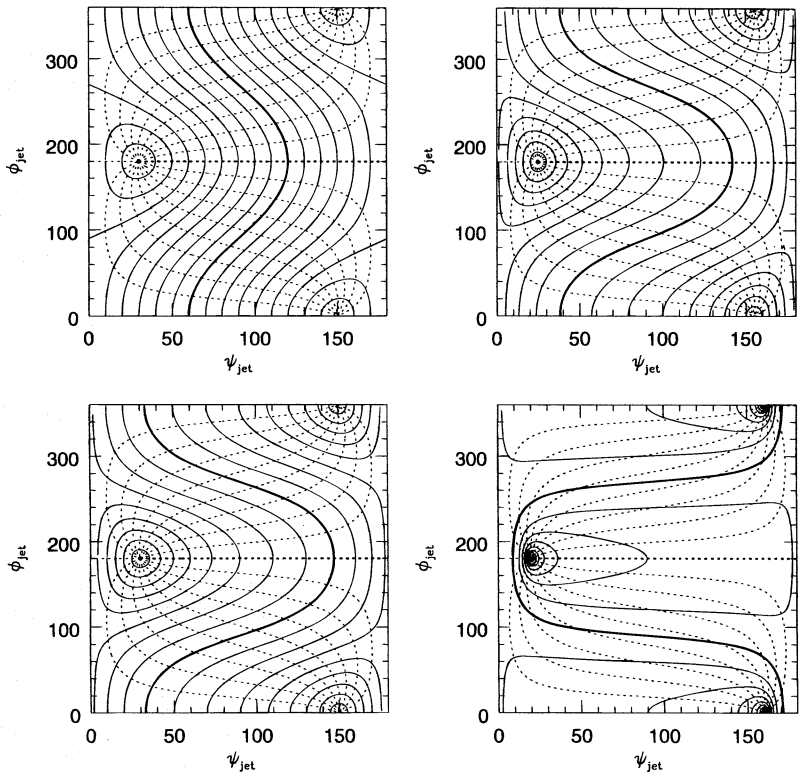

FIG. 3.—Contour plots of the polar angles ψ_{obs}, ϕ_{obs} describing the apparent orientation of the shock normal in the observer's frame, as a function of the intrinsic orientation in the jet frame for various values of the apparent shock velocity and viewing angle. Contours of ψ_{obs} (*solid lines*) give the apparent tilt of the shock out of the plane of the sky, while contours of ϕ_{obs} (*dotted lines*) give the apparent position angle of the shock normal with respect to the projected jet axis. The ψ_{obs} contours are plotted every 10°, with edge-on shocks denoted by a heavy solid contour; ϕ_{obs} contours are plotted every 20°. *Upper left*: $\beta_a = 0$, $\theta = 30°$; *top right*: $\beta_a = 0.509$, $\theta = 25°$; *lower left*: $\beta_a = 0.509$, $\theta = 30°$; *bottom right*: $\beta_a = 5$, $\theta = 20°$.

angle of the shock velocity to the line of sight. These curves are parameterized by the *observed* shock angle $\psi_{obs} \sim 90°$ and correspond to a fixed values of the (observed) azimuthal angle $\phi_{obs} \approx 18°$ and $\beta_a = 0.51$. It can be seen here that for $\psi_{obs} \approx 90°$ the implied obliquity in the jet frame can be significant—approximately 40° when $\theta = 30°$. It is also obvious that the range of implied values of ψ_{jet} is quite large for a modest change in the observed direction of the normal with respect to the observer, reflecting the contour dilation in the neighborhood of $\psi_{obs} = 90°$ shown in Figure 3.

The right-hand panel of Figure 4 shows the dependence of the normal component of shock velocity, β_n, on θ. This is relevant to the solutions of the Rankine-Hugoniot equations discussed below. Note that for a perfectly edge-on shock, the value of β_n is independent of θ. This result can be derived analytically (see § A2).

3.2. *The Intrinsic Obliquity of the Knot A Shock*

Our discussion above of the geometry and kinematics of knot A suggests that the shock normal is oblique with respect to the flow. The relevant equations for oblique relativistic shocks are summarized in the Appendix.

The shock junction conditions for an oblique shock are most readily applied in a stationary-shock frame that is

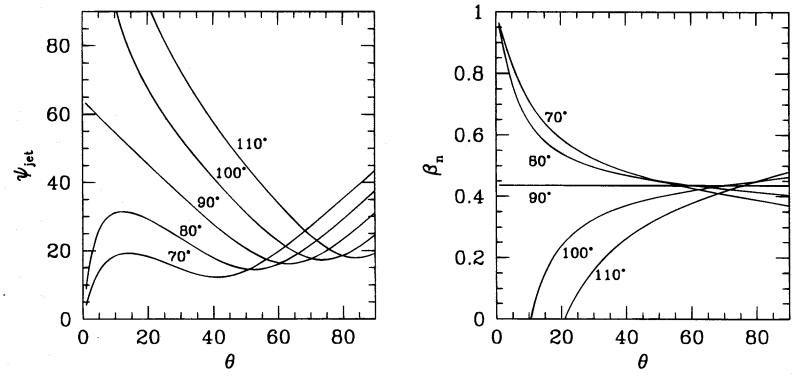

FIG. 4.—*Left*: Polar angle ψ_{jet} of the shock front (in the jet frame) as a function of the angle θ between the observer and the direction of the shock velocity, for the indicated values for the polar angle ψ_{obs} (in the observer's frame) of the apparent shock front. *Right*: Normal component of the velocity of knot A (in the jet frame) corresponding to the indicated values of ψ_{obs}. The observed value of the proper motion of knot A, $\beta_a \approx 0.509$ (Biretta, Zhou, & Owen 1995) was assumed here.

related to the jet frame by a boost of magnitude $\beta_n = \beta_p \cos \psi_{\rm jet}$ parallel to the shock normal $\boldsymbol{n}$ (see § A4, in particular § A4.2). The angles used to describe the shock and flow geometry are illustrated in Figures 5 and 6.

In our analysis, the jet axis $\boldsymbol{k}_{\rm jet}$ is identified with the direction of propagation of the shock. This direction is not exactly equal to the direction of either the pre- or the post-shock plasma, although one expects these three directions to be close, since the observed deflection is small. Once we fix the apparent speed β_a and position angle $\phi_{\rm obs}$ of the shock, as observations permit us to do for knot A ($\beta_a = 0.509$, $\phi_{\rm obs} = 18°$), we can seriously constrain the various angles describing the intrinsic properties of the shock (see

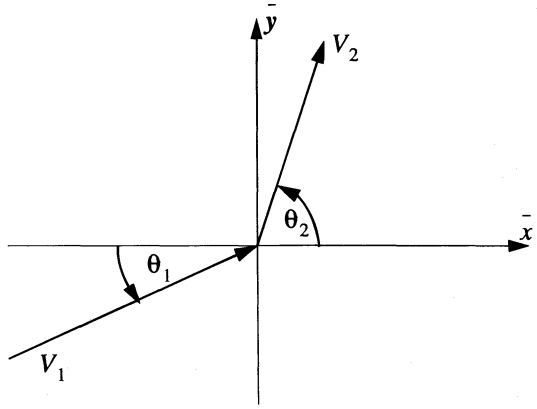

FIG. 5.—Coordinate system for oblique shocks in the shock rest frame

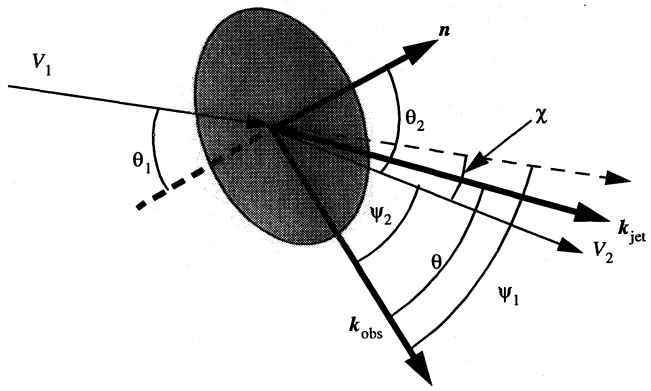

FIG. 6.—Definitions of the angles discussed in the text relating to oblique shocks in jets.

§ A4.1). In Figure 7 various shock-related angles are plotted against ψ_1, the angle between the preshock plasma velocity and the observer direction (see Fig. 6), for different values of θ and for a nominal deflection angle $\chi = \theta_2 - \theta_1 = 5°$.

The main result of interest here is the curve describing the angle, θ_1, between the preshock plasma and the shock normal, since this defines the intrinsic obliquity of the shock. The various panels of Figure 7 show the results for an apparently edge-on shock (i.e., $\psi_{\rm obs} = 90°$) with $\theta = 25°$, 30°, 35°, and 40°. Note that the projected deflection (calculated from the difference in azimuthal angles of the pre- and postshock velocities in the observer's coordinate system) is a signed quantity and that the negative values in

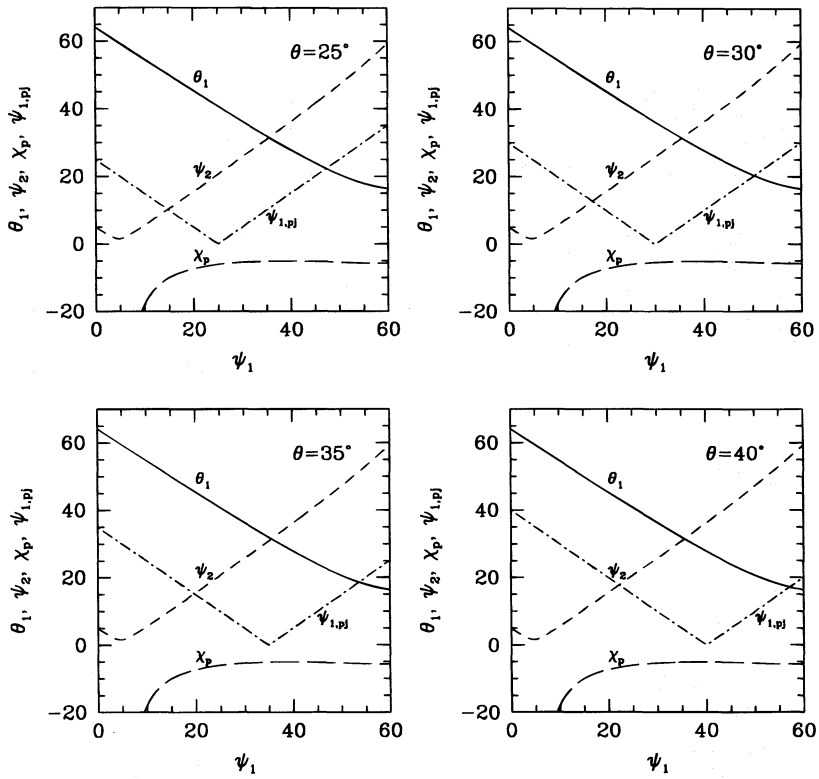

FIG. 7.—Relationships among the angles characterizing the knot A shock ($\beta_a = 0.509$, $\phi_{\rm obs} = 18°$), assuming edge-on appearance ($\psi_{\rm obs} = 90$) and indicated values of the angle θ between the observer's line of sight and the jet axis. In all cases the angular deflection across the shock is assumed to be $\chi = 5°$. The following angles are plotted against ψ_1, the angle between the upstream flow and the observer's line of sight: $\psi_{1,pj}$, the angle between the preshock plasma and the shock direction in the jet frame; ψ_2, the angle between the observer's line of sight and the direction of the postshock plasma; χ_p, the projected deflection angle of the plasma; and θ_1, the angle between the preshock plasma and the shock normal.

all panels of Figure 7 imply that the apparent deflection of the jet is to the south on the sky plane—as observed.

Concentrating on those shocks for which the angle between the preshock plasma and the observer is close to the angle between the shock direction and the observer (i.e., $\psi_1 \approx \theta$) shows that θ_1 increases as θ decreases, implying that the inferred obliquity of knot A varies inversely with the angle θ at which we view the M87 jet. However, note that, for $\theta = 25°$, the projected jet deflection across the shock increases quite rapidly for only a moderate decrease in ψ_1. The angle θ_1 is also quite sensitive to ψ_{obs}, i.e., to departures from an edge-on viewing angle. Figure 8 shows the result for $\psi_{obs} = 100°$ and $\theta = 30°$. The effect of this slight change of observed orientation is to make the shock more oblique, i.e., θ_1 increases. Thus, for $\theta = 30°$, θ_1 ranges from about 35° for $\psi_{obs} = 90°$ to about 53° for $\psi_{obs} = 100°$. It is shown below that this difference is quite significant when making comparisons with the Mach angle.

3.3. *Implications of Shock Junction Conditions*

Let us now consider the implications of the shock junction conditions for the shock pressure ratio, the postshock velocity, and the deflection angle of the plasma. These parameters are calculated through transformations between the jet frame and a shock frame via a boost of magnitude equal to the normal component, β_n, of the shock velocity in the direction of the shock normal. The detailed implementation of the shock junction conditions is summarized in § A4.2.

When the apparent shock normal is exactly perpendicular to the line of sight ($\psi_{obs} = 90°$),

$$\beta_n = \beta_a \frac{\cos \phi_{obs}}{(1 + \beta_a^2 \cos^2 \phi_{obs})^{1/2}} \tag{3.5}$$

and is independent of θ (see § A2). For knot A, $(\beta_a, \phi_{obs}) = (0.509, 18°)$, implying $\beta_n \approx 0.44$. For shocks that are not apparently edge-on, β_n depends upon θ; this dependence is shown in the right-hand panel of Figure 4.

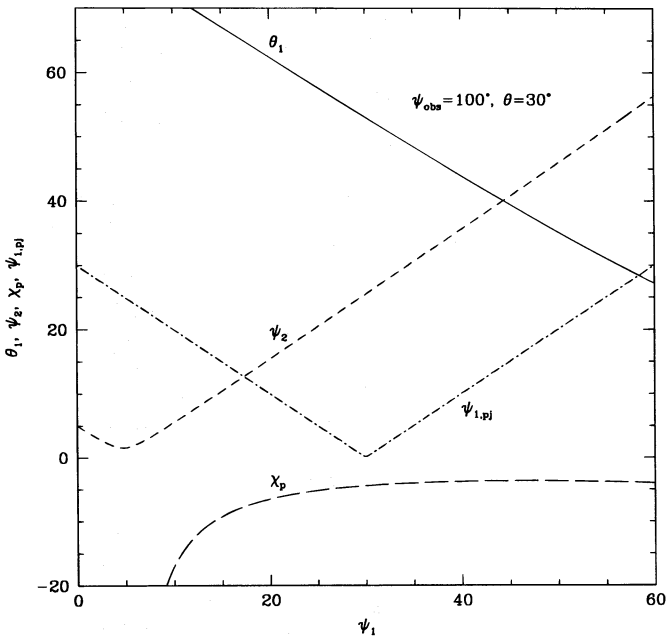

FIG. 8.—Same as Fig. 7, but for a polar angle of the apparent shock normal, ψ_{obs}, equal to 100°.

The parameters of interest to the problem are the following:

1. The ratio p_2/p_1 of postshock to preshock pressure. It has been well known, principally since the work of Norman, Winkler, & Smarr (1984), that shocks can lead to regions of transient overpressure in jets. Hence it is not surprising to find that the minimum synchrotron pressures of the knots exceed the pressure in the ambient interstellar medium. However, the ratio of postshock to preshock pressure may not be as great as first thought if the radio lobe itself is also overpressured. Indeed this is proposed in § 6, and, as we have seen in § 2, such a proposition is consistent with the observations. Hence, although the knot A minimum pressure exceeds that of the surrounding ISM by a factor ~ 8 (assuming a uniform emissivity) (Owen et al. 1989), p_2/p_1 may be somewhat lower. Some indication of the pressure jump may be obtained from the ratio of the knot A minimum pressure to the pre–knot A value, which gives $p_{2,min}/p_{1,min} \approx (I_2/I_1)^{4/7} \approx 5$–6, where I_2 and I_1 are the relevant surface brightnesses. We also note that the estimated minimum pressure varies with the Doppler factor, $\mathscr{D}$, according to $p_{min} \propto \mathscr{D}^{-2(\alpha+2)/(\alpha+3)} \approx \mathscr{D}^{-1.43}$ for M87, so that relativistic corrections can be important at the level of about a factor of 2. Given that $\theta \lesssim 35°$, such corrections are most important for the lower Lorentz factors $\gamma \approx 3$–5, so they are likely to affect the downstream region more than the upstream region. This implies that the ratio of knot A pressure to that of the ISM may be even lower.

2. The angle θ_1 between the preshock plasma and the shock normal. This needs to be consistent with the range of values inferred above from the appearance of knot A.

3. The postshock Lorentz factor, γ_2. Depending on the shock angle, θ_1, this may be considerably lower than the preshock Lorentz factor. The consequence of this would be a reduction in the amount of beaming. As we pointed out earlier, one can see that $\gamma \gtrsim 2$ is required, assuming that the counterjet contains embedded structures similar to the knots in the main jet.

4. The deflection of the jet in the plane of the sky, χ_p. This is only 5°–6° following knot A; it is important to reconcile such a small deflection with a moderate pressure jump. Plotting deflection angle against the angle between the preshock plasma and the line of sight, ψ_1, shows that, for the line-of-sight angles considered here, the *projected* deflection does not differ much from the intrinsic deflection angle, χ. Typically it is only slightly less, in some cases by a degree or so. This means that in the following we will not rigorously distinguish between projected and intrinsic values of this angle.

Figures 9–12 summarize the results of solving the relativistic Rankine-Hugoniot equations (see § A4.2) for various values of the pre-shock Lorentz factor, $\gamma_1 = 3$, 5, 7, 9, and for values $\mathscr{R}_j = \rho c^2/4p = 0$, 1, 2, and 4 of the ratio of cold matter rest-mass energy density to enthalpy. The abscissa for the curves shown in the left-hand panels of these figures is θ_1, the angle between the preshock fluid and the shock normal, as measured in the jet frame. All curves show the characteristic behaviors associated with oblique shocks. The pressure ratio is a maximum for normal shocks and diminishes to unity at the Mach angle, while the postshock Lorentz factor is lowest for normal shocks and is equal to the preshock Lorentz factor at the Mach angle. Curves of θ_1 and pressure ratio versus deflection angle are

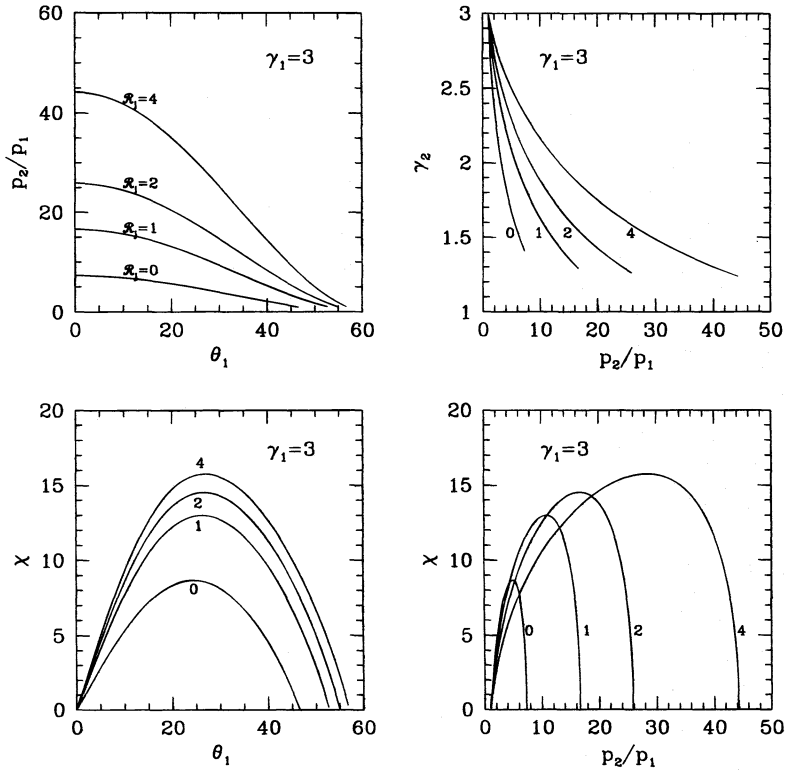

FIG. 9.—Solutions of the relativistic Rankine-Hugoniot equations for a preshock Lorentz factor, $\gamma_1 = 3$, and values of $\mathcal{R}_j = 0, 1, 2, 4$. *Upper left*: ratio of postshock to preshock pressure vs. the angle θ_1 between the preshock plasma velocity and the shock normal; *upper right*: postshock Lorentz factor γ_2 vs. the shock pressure ratio; *lower left*: deflection angle vs. the shock angle θ_1; *lower right*: deflection angle vs. shock pressure ratio.

formally double-valued, but it seems to be at least empirically established that for fixed deflection angle χ the solutions with larger obliquity (and lower pressure jump) are selected by nature (see, for example, § 92 of Landau & Lifshitz 1987). The top right-hand panel of each set of plots shows the postshock Lorentz factor as a function of pressure ratio, and the bottom right-hand panels show the very useful diagnostic of deflection angle versus pressure ratio.

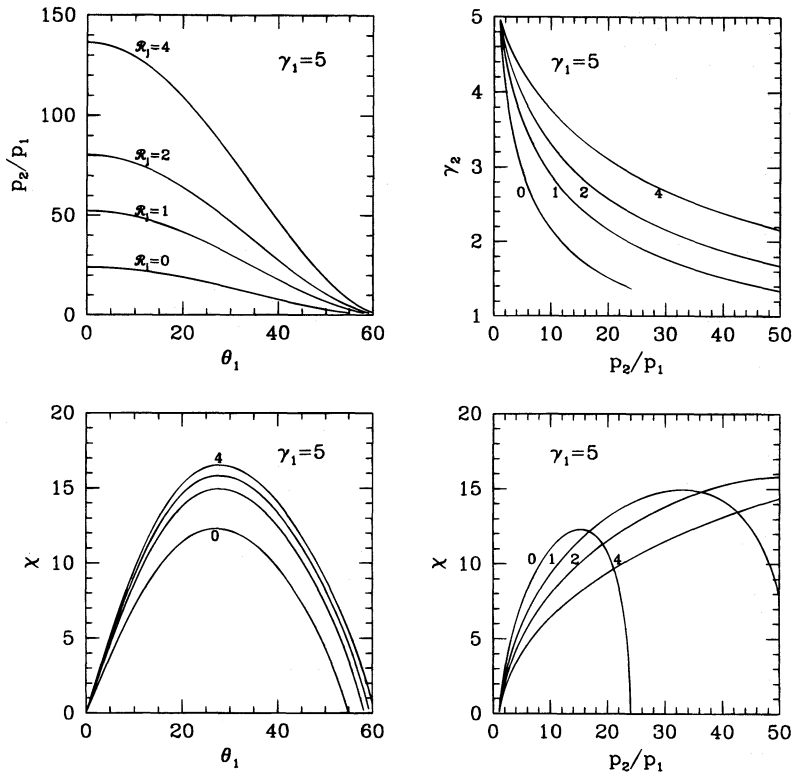

FIG. 10.—Same as Fig. 9, but for $\gamma_1 = 5$

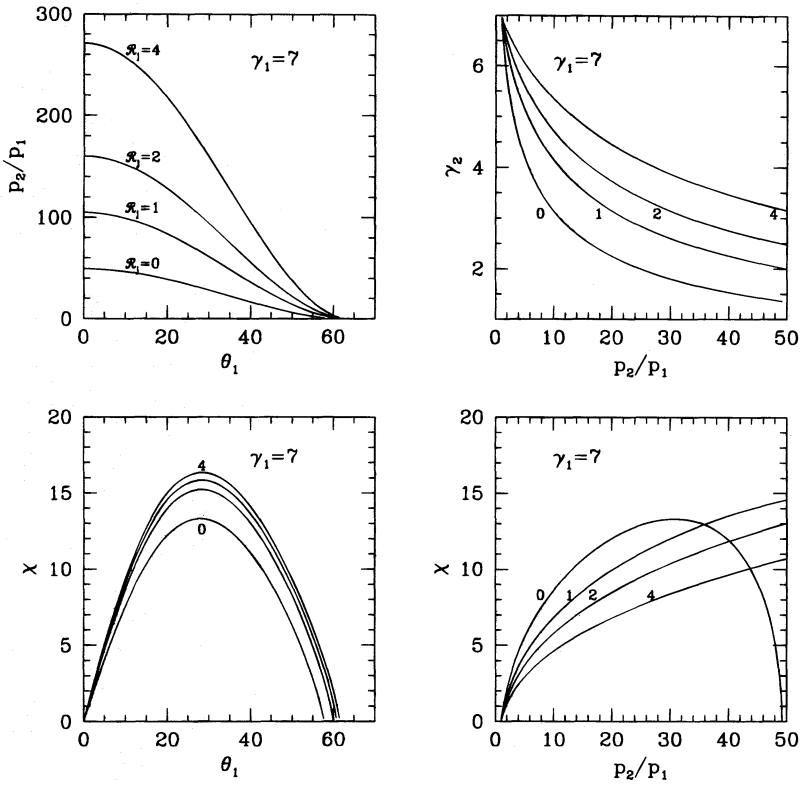

FIG. 11.—Same as Fig. 9, but for $\gamma_1 = 7$

The Mach angle for each shock model is identified by the value of θ_1 at which the pressure ratio p_2/p_1 is unity, that is, the right-hand end of the curve of p_2/p_1 versus θ_1.

Features of interest in these diagnostic curves include (1) higher pressure ratios for angles close to the Mach angle when the amount of cold matter increases and (2) a fairly strong change in the dependence of the deflection angle on pressure ratio with increasing $\mathscr{R}$. Also note that for most of the cases presented, $p_2/p_1 \lesssim 5$–10 when $35° \lesssim \theta_1 \lesssim 50°$, compatible with the angles inferred from knot A's appear-

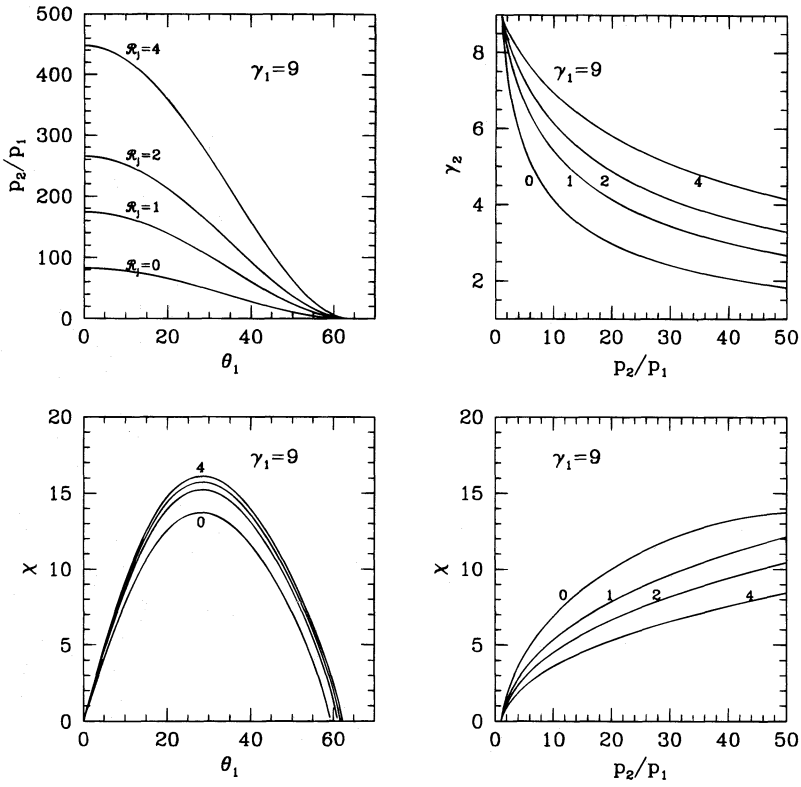

FIG. 12.—Same as Fig. 9, but for $\gamma_1 = 9$

ance and kinematics when the shock velocity makes an angle to the line of sight of $\theta \sim 30°$. Thus, consistency between the shock dynamics and relativistic kinematics is established for a viewing angle of this magnitude. This is independent of constraints based upon counterjet to main jet surface brightness ratios and therefore indicates that the theory developed so far is substantially consistent.

Given the nature of the observational constraints, it is difficult to constrain Lorentz factors and rest mass to enthalpy ratios from shock solutions alone. However, some interesting trends are evident which we briefly note here, focusing in particular on the relationship between pressure ratio and deflection. If the shock pressure ratio is about 5 and the deflection about 5°, then for $\gamma_1 = 3$ we require $\mathscr{R}_j \gtrsim 4$. This decreases to $\mathscr{R}_j \approx 1$ for $\gamma_1 = 5$, to $\mathscr{R}_j \approx 0$ for $\gamma_1 = 7$, and there is no solution for $\gamma_1 = 9$. If, on the other hand, $p_2/p_1 = 10$, then we have $\mathscr{R}_j \gtrsim 4$ for $\gamma_1 = 3$ and 5, $\mathscr{R}_j \approx 2$ for $\gamma_1 = 7$, and $\mathscr{R}_j \approx 1$ for $\gamma_1 = 9$. That is, as the Lorentz factor increases, the constraints on the shock pressure ratio and deflection are satisfied by shocks with less cold matter, simply reflecting the dependence of the energy and momentum flux on the jet inertia. A further point worth emphasizing from these diagrams is that the dependence of deflection angle and postshock Lorentz factor on pressure jump is quite sensitive, so that if the pressure ratio at knot A is actually less than 5, a Lorentz factor as low as 3 is feasible. This is relevant to the constraints placed upon the jet energy flux (which is proportional to γ^2) by the dynamics of the bubble (see § 6).

What could cause a sequence of oblique shocks to form? In the next section we show that both the spacing and the proper motions of the M87 knots are consistent with the bending resulting from helical ($m = 1$) Kelvin-Helmholtz instabilities, provided that the density in the surrounding medium is not too large with respect to the proper density of the jet.

Virtually all of the above theory has been directed at the dynamics of knot A, since, as a result of its fortuitous edge-on appearance, its parameters are better constrained than those of the other knots. Qualitatively, however, similar relationships among deflection angle, pressure ratio, and postshock Lorentz factor should hold at the knots beyond knot A. The knots upstream of knot A appear to be highly oblique, so that the pressure jumps are correspondingly small and the knots are not as bright. The appearance of the complex of knots starting at knot D is also similar to the knot A-B-C complex, with the qualification that knot D does not appear as edge-on as knot A.

4. PRODUCTION OF SHOCKS VIA THE KELVIN-HELMHOLTZ INSTABILITY

The M87 jet clearly oscillates beyond knot A before it bends and merges into the northwest lobe. It is appealing to interpret these oscillations as being related to the helical ($m = 1$) Kelvin-Helmholtz instability, as did Hardee (1982). The major differences between the following and Hardee's analysis is that we assume that the jet is relativistic and allow the density surrounding the jet to be quite different from that of the ISM.

A major idea developed in this section is that the bending of the supersonic flow induced by this instability is responsible for the development of quasi-periodic shocks which eventually disrupt the jet. This means that the pattern speed of the shocks (knots) must be the same as the pattern speed of the instability and that this constraint together with the observed wavelengths can further constrain the parameters of the jet and the surrounding medium.

Hardee (1982) fitted an exponentially growing wave to the Owen, Hardee, & Bignell (1980) 15 GHz data to obtain a wavelength of $8\farcs5 \approx 12.3$ jet radii with an e-folding length of $6\farcs5 \approx 10$ jet radii. Visual inspection of the more recent data (e.g., Owen et al. 1989) for the largest amplitude oscillations confirms that the wavelength of the oscillations is indeed of order 10 jet radii. Allowing for the fact that the jet is observed at approximately 30°–40° to the line of sight, the unstable wavelength is probably closer to ~ 25 jet radii and, similarly, the actual e-folding length is approximately 20 jet radii. The purpose of this section is to compare these e-folding lengths and wavelengths to the values predicted by linear Kelvin-Helmholtz theory for a cylindrical jet (Birkinshaw 1984; Hardee 1987a, 1987b). Following Birkinshaw (1984), we adopt a spatial instability analysis (real frequency and complex wavenumber), since this allows us to track the growth of arbitrary time-dependent perturbations introduced at an arbitrary point along the jet. We then search for the mode with the maximum growth rate.

Birkinshaw (1984) derived a dispersion relation for a relativistically moving jet with a nonrelativistic equation of state. Fortunately, it is easy to modify the dispersion equation to allow for a relativistic equation of state. The modification to the dispersion relation consists of replacing the nonrelativistic sound speed squared, $c_s^2 = \Gamma p/\rho$, by its relativistic counterpart $\beta_s^2 = c_s^2/c^2 = 3^{-1}(1 + \rho c^2/4p)^{-1}$ for both the jet and the ambient plasma. This expression for the sound speed is relevant when the internal energy is dominated by relativistic particles. We assume that this is the case in both the jet and the ambient plasma and the reason for this is evident below.

The modified dispersion relation for perturbations proportional to $\exp[i(kz + m\phi - \omega t)]$ can be written in the following form:

$$\frac{H_m^{(1)\prime}(\alpha_a R)}{H_m^{(1)}(\alpha_a R)} \frac{(\beta_{\rm ph}^2/\beta_{s,a}^2 - 1)^{1/2}}{(1 + \mathscr{R}_a)\beta_{\rm ph}^2} = \frac{J_m'(\alpha_j R)}{J_m(\alpha_j R)} \frac{[(\beta_{\rm ph} - \beta)^2/\beta_{s,j}^2 - (1 - \beta\beta_{\rm ph})^2]^{1/2}}{(1 + \mathscr{R}_j)\gamma(\beta_{\rm ph} - \beta)^2}, \quad (4.1)$$

$$\alpha_a R = \left(\frac{\omega R}{c}\right)\beta_{\rm ph}^{-1}\left(\frac{\beta_{\rm ph}^2}{\beta_{s,j}^2} - 1\right)^{1/2}, \quad (4.2)$$

$$\alpha_j R = \left(\frac{\omega R}{c}\right)\gamma\beta_{\rm ph}^{-1}\left[\frac{(\beta_{\rm ph} - \beta)^2}{\beta_{s,j}^2} - (1 - \beta\beta_{\rm ph})^2\right]^{1/2}. \quad (4.3)$$

The above formulation generally follows Birkinshaw's notation in which subscripts a and j refer to the ambient medium and the jet, respectively, ω is the (real) frequency, $k = k_r + ik_i$ is the (complex) wavenumber, $\beta_{\rm ph} = \omega/k$ is the (complex) phase velocity, and R is the jet radius. As in the previous section, the parameters $\mathscr{R}_{(a,j)} = \rho_{(a,j)}c^2/4p_0$, where p_0 is the zeroth-order pressure, represent the ratio of cold matter energy density to enthalpy in both media.

Since the frequency, ω, of the perturbation is real, the complex spatial wavenumber is calculated from the complex phase velocity by

$$kR = k_r R + ik_i R = \frac{\omega R/c}{\beta_{\rm ph}}. \quad (4.4)$$

The growth length of the perturbation is defined as $\lambda_g = k_i^{-1}$, and the wavelength is $\lambda_0 = 2\pi/k_r$. Growing waves are characterized by $k_i < 0$. We define the real phase velocity by $v_{\rm ph} = \omega/k_r$ and formally define a group velocity by $v_g = d\omega/dk_r = v_{\rm ph} + k_r\, dv_{\rm ph}/dk_r$. The waves are highly unstable, with e-folding lengths comparable to their wavelengths, and the usefulness of the concept of group velocity for such rapidly growing waves is somewhat dubious. However, as we see below, the phase and group velocities do not differ greatly, and it is reasonable to assume that they give a satisfactory indication of the speed of propagation of the instability. This is especially the case at the maximally growing wavelength, which occurs at the minimum of the phase velocity and where the phase and group velocities are identical.

There are readily identifiable low- and high-frequency limits to the above dispersion equation. For low ω and $m = 1$, the phase velocity corresponding to growing modes is

$$\beta_{\rm ph} = \beta\left[\frac{1}{1 - i\gamma^{-1}(1 + \mathcal{R}_a)^{1/2}/(1 + \mathcal{R}_j)^{1/2}}\right]. \quad (4.5)$$

In this limit the relationship between growth length and wavelength is linear:

$$\lambda_g \approx \left[\frac{\gamma}{2\pi}\left(\frac{1 + \mathcal{R}_j}{1 + \mathcal{R}_a}\right)^{1/2}\right]\lambda_0\,. \quad (4.6)$$

The high-frequency limit for the phase velocity is

$$\beta_{{\rm ph},\pm} = \frac{\beta \pm \beta_{s,j}}{1 \pm \beta\beta_{s,j}} \quad (4.7)$$

and is real. These solutions represent sound waves traveling in the jet direction (plus sign) or opposite to the jet (minus sign). In numerically solving the dispersion equation, we begin with the low-frequency limit representing growing waves, and progress toward high frequency, using a Newton-Raphson technique. The high-frequency numerical solution converges to $\beta_{{\rm ph},-}$. This corresponds to sound waves in the jet attempting to resonate with sound waves in the background medium by traveling counter to the jet direction.

We have solved the dispersion equation numerically for a number of Lorentz factors of interest, and for various values of $\mathcal{R}_a$ and $\mathcal{R}_j$. A set of such solutions for $\gamma = 5$ is represented in Figures 13 and 14. In Figure 13 the growth length is plotted against the wavelength of the perturbation. Each panel corresponds to one of the four different values of $\mathcal{R}_j$ used in the previous section, i.e., $\mathcal{R}_j = 0$, 1, 2, 4. The three curves in each panel correspond to different values of the ratio of the ambient rest mass to enthalpy, $\mathcal{R}_a = 0$, 10, 25. The feature that all these curves have in common is a fairly broad minimum identifying the most unstable modes. Note also the linear relationship between λ_g and λ_0 for long wavelengths, which is well described by equation (4.6).

Examination of Figure 13 shows that for fixed $\mathcal{R}_a$ the most unstable modes occur when the *jet* plasma is highly relativistic ($\mathcal{R}_j = 0$), and for fixed $\mathcal{R}_j$ the most unstable modes occur when the *ambient* plasma is highly relativistic ($\mathcal{R}_a = 0$). Note that it is relatively easy to find unstable modes whose wavelengths are close to that of the M87 jet. For example, for $(\mathcal{R}_j, \mathcal{R}_a) = (4, 25)$ the maximally growing wavelength is near 25 jet radii with a corresponding growth length near 20 jet radii. This raises the question of how to compare these linear solutions with the observations, since in the view we are promoting here, shock waves have saturated the instability. The maximally growing *wavelength* of the linear instability should correspond to the observed wavelength of the unstable jet, since the latter would have

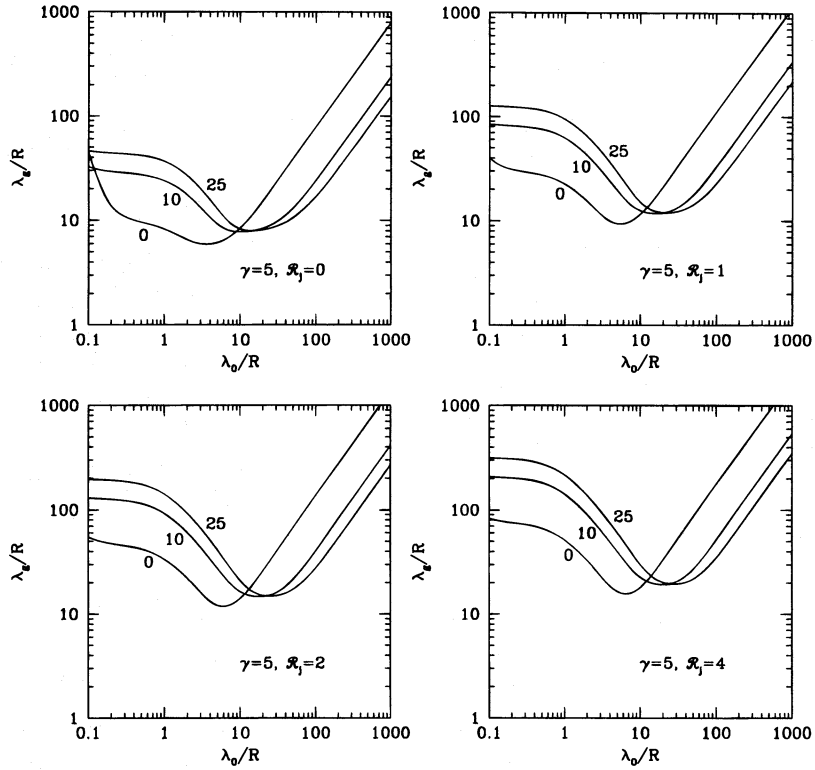

FIG. 13.—The e-folding length, λ_g, vs. wavelength, λ_0, derived from the dispersion relation for the helical ($m = 1$) Kelvin-Helmholtz instability, for a jet with Lorentz factor $\gamma = 5$ and $\mathcal{R}_j = 0$, 1, 2, 4. The value of $\mathcal{R}_a$ is indicated on each curve.

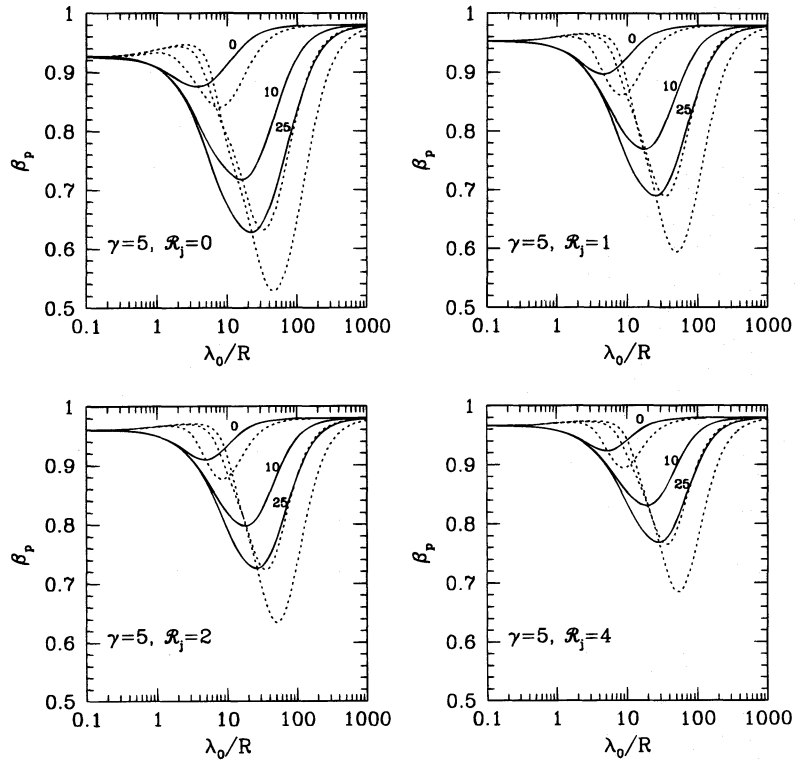

FIG. 14.—Phase and group velocities corresponding to the unstable modes plotted in Fig. 13. The dotted curves are the group velocities corresponding to each value of $\mathcal{R}_a$. Each group velocity curve passes through the minimum of the corresponding phase velocity curve.

developed from the most rapidly growing linear modes. However, the spatial *rate* of growth will have been damped by the resultant shock waves, and therefore the observed growth wavelength is likely to be longer than that calculated from linear instability theory. In the linear phase the pattern speed is independent of the amplitude of the instability, so that when the shocks form at the bends of the jet their initial speed should be equal to the instability pattern speed. We therefore assume that, as the shocks develop, their pattern speed is maintained near the pattern speed of the linear instability. It will be useful to check these assertions with three-dimensional hydrodynamic simulations.

The phase and group pattern speeds for the $\gamma = 5$ jet are shown in Figure 14. The general features of the curves of phase speed are the short-wavelength (high-frequency) and long-wavelength (low-frequency) limits described above and a pronounced minimum at the point of maximum growth. The minimum velocity therefore represents the velocity of the maximally growing wave and is the velocity most likely to be observed. The corresponding group speeds are also shown as a function of wavelength. However, as noted above, these are equal to the phase speeds at the minimum point.

Other general features of the helical Kelvin-Helmholtz instability which are evident from these curves are (1) the reduction in the pattern speed as the ambient density (i.e., $\mathcal{R}_a$) increases and (2) the increase in the pattern speed as the jet density (i.e., $\mathcal{R}_j$) increases.

In order to gain an appreciation of the way in which the relevant wavelengths and velocities depend upon jet parameters, we have plotted, in Figures 15 and 16, the growth lengths (λ_g) and wavelengths (λ_0) of the fastest growing waves as a function of $\mathcal{R}_a$ and the maximally growing wavelength as a function of the phase speed, β_p, for the same Lorentz factors as in the previous section, i.e., $\gamma = 3$, 5, 7, and 9. We have also indicated, on the $\lambda_0 - \beta_p$ plots, the locus of points implied by the observational data relevant to knot A, i.e., $\lambda_0/R \approx 12.3/\sin\theta$ and $\beta_p \approx 0.51/(\sin\theta + 0.51\cos\theta)$ with $25° \lesssim \theta \lesssim 40°$.

The plots of λ_0 versus β_p show an interesting trend with Lorentz factor. When $\gamma = 3$, the best-fit value is $\mathcal{R}_j \approx 2$; when $\gamma = 5$, it is $\mathcal{R}_j \approx 0.5$ and when $\gamma = 7$, it is $\mathcal{R}_j \approx 0$. There is no fit for $\gamma = 9$. The corresponding values of the e-folding length, λ_g, are approximately 9, 10, and 12, respectively, and are shorter than the value fitted by Hardee (1982), $\lambda_g/\mathcal{R} \approx 10/\sin\theta$. However, as discussed above, one expects such an effect due to saturation of the instability via shock waves.

It is possible to obtain estimates of jet parameters by comparing the shock solutions with the fits to the Kelvin-Helmholtz instability. The best-fit parameters are compared in Table 1, and it is evident that, given the assumptions entailed in the foregoing theory (principally the neglect of the magnetic field), the best-fit Lorentz factor is in the vicinity of 5–7 if the pressure jump at knot A is 5. Moreover, these comparisons do not support a pressure jump as high as 10. Obviously, if the pressure jump is lower than 5 (and

TABLE 1

COMPARISON OF KELVIN-HELMHOLTZ AND SHOCK PARAMETERS

LORENTZ FACTOR	KELVIN-HELMHOLTZ INSTABILITY		SHOCKS	
			$p_2/p_1 = 5$	$p_2/p_1 = 10$
3.....	$\mathcal{R}_j \approx 2$	$\lambda_g \approx 9$	$\mathcal{R}_j \gtrsim 4$	$\mathcal{R}_j \gtrsim 4$
5.....	$\mathcal{R}_j \approx 0.5$	$\lambda_g \approx 10$	$\mathcal{R}_j \approx 1$	$\mathcal{R}_j \gtrsim 4$
7.....	$\mathcal{R}_j \approx 0$	$\lambda_g \approx 12$	$\mathcal{R}_j \approx 0$	$\mathcal{R}_j \approx 2$
9.....	...	...	$\mathcal{R}_j \approx 0$	$\mathcal{R}_j \approx 0.5$

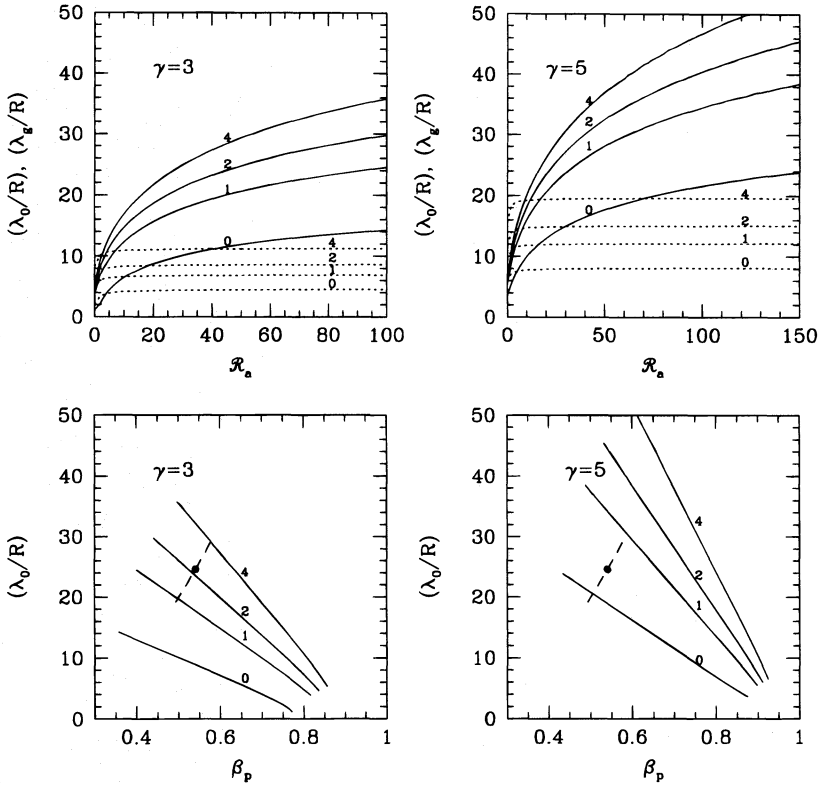

FIG. 15.—Upper panels show the wavelengths (*solid curves*) and *e*-folding lengths (*dotted curves*) as functions of $\mathcal{R}_a$ for the maximally growing helical waves in jets with Lorentz factors 3 and 5 and values of $\mathcal{R}_j = 0, 1, 2, 4$ as indicated. The lower panels show the wavelength plotted against the corresponding phase velocity (equal to the group velocity for the fastest growing wave). Also shown on these plots is the locus of (λ_0, β_p) implied by Hardee's (1982) fit to the jet center line and the proper-motion data of Biretta et al. (1995) for $25° < \theta < 40°$; θ increases from the top to the bottom of each curve, and $\theta = 30°$ is marked by a solid point.

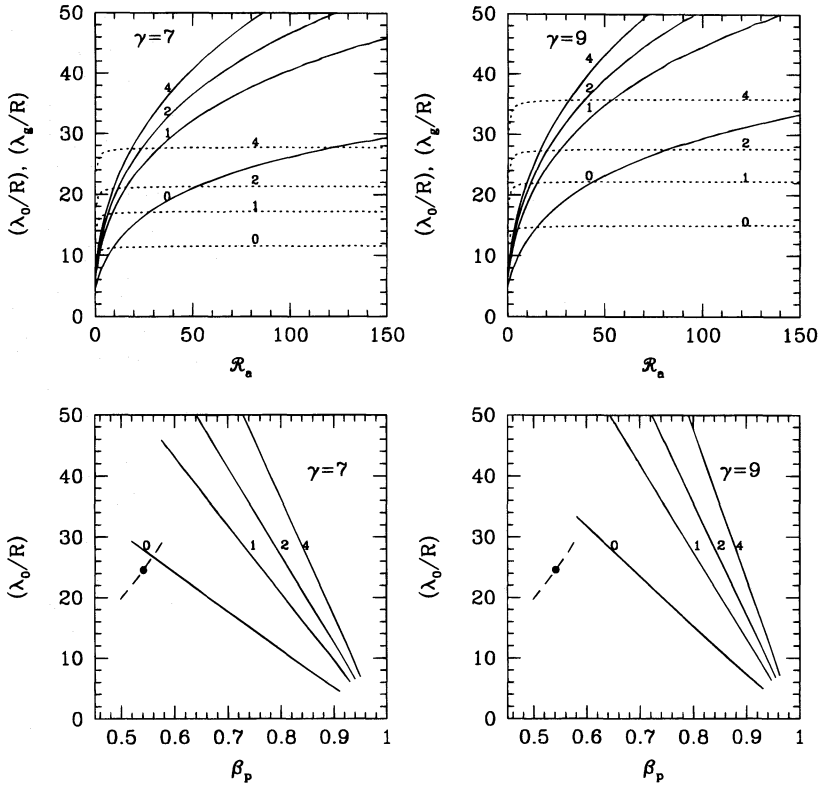

FIG. 16.—Same as Fig. 15, but for $\gamma = 7$ and 9

given that the deflection is quite a sensitive function of p_2/p_1), then the best-fit Lorentz factor is lower.

For all of the reasons expressed above, such estimates can only be regarded as indicative. However, it is of interest to note the consistency of a Lorentz factor ≈ 5 with the estimates of Padovani & Urry (1990) based upon unification of Fanaroff-Riley I radio galaxies with BL Lac objects.

An important and secure conclusion from the above analysis of the Kelvin-Helmholtz instability is that, irrespective of the actual value of the Lorentz factor, the density of the medium surrounding the jet is constrained by $10 \lesssim \mathscr{R}_a \lesssim 100$ with a corresponding number density $n_a \approx 4 \times 10^{-4}$ cm^{-3} $(\mathscr{R}_a/100)(p_a/10^{-9}$ dyn cm$^{-2})$. This is much less than the density $n_{\rm ISM} \sim 0.1$ cm^{-3} of the surrounding interstellar medium. The immediate implication of this is that the M87 jet is blowing a low-density, overpressured bubble into the interstellar medium of M87. On the other hand, the fact that the density of the bubble is at least 10 times higher than the density of the jet ($\mathscr{R}_a \gg \mathscr{R}_j$), for *all* possible fits to the data, implies that the bubble is contaminated to some extent by thermal material. There are two possible sources for this contamination: (1) leakage of ISM through the surface of the ISM-bubble interface and (2) stellar mass loss over the lifetime of the bubble. For future reference (in § 7), we note that the mass of thermal material in the lobe $M_{\rm th}$ is $\approx 5 \times 10^4 (\mathscr{R}_a/100) p_{-9}\, M_\odot$.

5. THE SPECTRA OF THE KNOTS

In the previous sections we have modeled the knots as shocks. It remains to be shown that this is consistent with *both* the radio and the optical appearance of the jet, especially in view of the striking similarity of the radio and optical images. As we remarked in § 2, the radio-optical ratio image reveals important differences between the radio and optical structure which, at least qualitatively, can be attributed to the effect of more rapid synchrotron cooling of the optically emitting electrons. In this section we show *quantitatively* that such an explanation is feasible by showing that the estimated break frequencies of knots A and B are consistent with the observations provided that one takes some care in estimating the cooling time corresponding to a given aperture. We restrict ourselves to knots A and B, since Biretta et al. (1991) determined radio to X-ray spectra for these knots using precisely defined apertures. They also determined an integrated spectrum for knot D; however, this involved the entire knot D complex, which, according to our interpretation of the knots, contains three shocks.

Our model for the knot spectra is as follows: High-energy electrons are reaccelerated at the shock front and cool downstream by synchrotron radiation. The spectrum of each knot is an integrated spectrum obtained from a fixed aperture that encompasses the immediate postshock region and the cooling region. There are two main features of the spectrum to be explained by such a model: one is the location of the break in the spectrum; the other is the magnitude of the break in the spectral index. If conditions following the shock are perfectly homogeneous (i.e., constant velocity, magnetic field, and number density), it is straightforward to show that the break in spectral index, $\Delta\alpha$, is precisely 0.5. If conditions are inhomogeneous, it is possible that $\Delta\alpha > 0.5$. For example, Coleman & Bicknell (1988) showed that inhomogeneous conditions following a fixed bow shock lead to $\Delta\alpha > 0.5$.

The magnitude of the break in the spectrum produced by moving shocks is unknown. However, it is clear that the *location* of the break is simply determined by the cooling timescale of electrons across the aperture. A naive calculation would involve comparison of the flow timescale d/c, where d is the size of the aperture, with the synchrotron cooling timescale $t_{\rm syn} \approx 1.6 \times 10^9\ B_{-6}^{-3/2}\ \nu_9^{-1/2}$ yr, where B_{-6} is the magnetic field in microgauss and ν_9 is the break frequency in gigahertz. It is well known that such a comparison produces a disparity in timescales; the timescale implied by the break frequency is at least a factor of a few shorter than the timescale implied by the size of the aperture. However, there are a number of effects to take into account. These are (1) the time dilation of the relativistically moving plasma, (2) time retardation, (3) the relative velocity of the shocked plasma with respect to the shock, (4) the blueshift of the spectrum, and (5) the effect of relativistic beaming on estimates of the equipartition magnetic field. Effects 1–4 are encapsulated in Figure 17. It is shown in the Appendix (§ A3) that the proper time, corresponding to the observed aperture, is

$$\tau = \frac{d}{c \sin\theta} \frac{1 - \beta_p \cos\theta}{\gamma(\beta - \beta_p)}, \tag{5.1}$$

where, as previously, β is the plasma speed, β_p is the speed of the shock, and θ is the inclination of the shock and plasma velocities to the line of sight. (For the purposes of this calculation, it is assumed that the postshock plasma velocity and the shock velocity are parallel.)

The synchrotron cooling timescale in the plasma rest frame, corresponding to the equipartition magnetic field B,

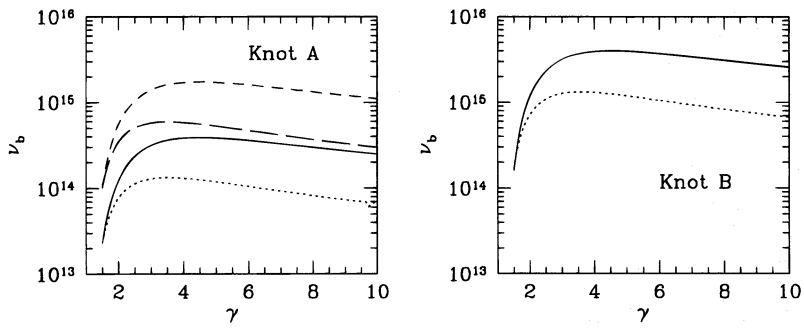

FIG. 17.—Estimated break frequency for knots A and B. The parameters for the curves are as follows. *Knot A, solid curve*, $B = 510$ μG, $\theta = 30°$; *short dashed curve*, $B = 510$ μG, $\theta = 40°$; *medium-dashed curve*, $B = 320$ μG, $\theta = 30°$; *long-dashed curve*, $B = 320$ μG, $\theta = 40°$. *Knot B, solid curve*, $B = 280$ μG, $\theta = 30°$; *short-dashed curve*, $B = 280$ μG, $\theta = 40°$. The magnetic field here refers to equipartition estimates uncorrected for relativistic effects.

is given by

$$t_{\rm syn} \approx 1.38 \times 10^{12} \mathscr{D}^{(4\alpha+9)/[2(\alpha+3)]} B_{\rm eq}^{-3/2} \nu_{\rm obs}^{-1/2} \ {\rm s} \ , \quad (5.2)$$

where $B_{\rm eq}$ is calculated without taking relativistic beaming into account, $\nu_{\rm obs}$ is the observed frequency (in Hz), the power of the Doppler factor $\mathscr{D}$ accounts for the relativistic correction to the equipartition magnetic field and the blueshift, and α is the low-frequency spectral index. The frequency at which the spectrum breaks, ν_b, is therefore given by equating τ to the synchrotron cooling time, so that

$$\nu_b \approx \frac{1.90 \times 10^{24}}{(d/c)^2} \frac{\gamma^2(\beta - \beta_p)^2 \sin^2\theta}{(1 - \beta_p \cos\theta)^2} \mathscr{D}^{(4\alpha+9)/(\alpha+3)} B^{-3} \ {\rm Hz} \ . \quad (5.3)$$

The break frequency is plotted as a function of the postshock Lorentz factor in Figure 17 for parameters appropriate for knots A and B. The sizes of the apertures are those employed by Biretta et al. (1991) (189 and 139 pc, respectively). Values of the equipartition magnetic field were taken from Owen et al. (1989) with two values for knot A (510 and 310 μG) corresponding to different slices through that knot. Break frequencies for two different orientations ($\theta = 30°$ and 40°) are plotted.

The actual observed break frequency is uncertain, perhaps by as much as an order of magnitude (cf. Biretta et al. 1991 and Meisenheimer, Röser, & Schlötelburg 1996). However, we shall take it as being in the range of $10^{14.5}$–10^{15} Hz. As one can see from these plots, the observed and predicted break frequencies are quite consistent for most of the plotted curves, although it is of interest to note that the break frequency becomes quite low for $\gamma \lesssim 2$, consistent with our earlier constraints on the postshock Lorentz factor. The curve which is *not* consistent is the lowest curve for knot A, for which $\theta = 40°$ and $B = 510$ μG. Again this is consistent with the earlier sections, since we favor $30° \lesssim \theta \lesssim 35°$.

Thus the observed break frequencies in knots A and B are consistent with what is inferred from our model, if the magnetic fields are near the equipartition value. It remains to be shown that the magnitude of the break in spectral index can be produced by such a model. This is deferred to future work.

6. INTERACTION BETWEEN THE INNER RADIO LOBES AND THE OPTICAL FILAMENTS

In § 4 we deduced that the inner radio lobes would have to be almost devoid of thermal plasma (compared to the density in the background "cooling flow") in order for the oscillations of the jet, and the spacing and motion of the knots, to be interpretable as the result of a Kelvin-Helmholtz instability. This implies that the radio lobes are bubbles expanding into the local ISM, with their expansion driven by the supply of internal energy from the jets. In this section we show that this idea is consistent with the inferred pressure, expansion timescale, and size of the bubble, and that the energy of expansion of this bubble is sufficient to excite the optical emission-line filaments discovered by Ford & Butcher (1979) and observed in greater detail by Sparks et al. (1992) (see § 2).

6.1. *Lobe Expansion*

The following approximate analysis of the expansion of an overpressured lobe is based, in part, on the corresponding analysis of adiabatic stellar wind-blown bubbles by Weaver et al. (1977). The major difference is that in our case the bubble is inflated by thermalized energy from a relativistic jet, whereas a wind-blown bubble is inflated by the thermalized kinetic energy of a spherically symmetric stellar wind.

As a realistic first approximation, we neglect effects due to the net momentum of the jet. This is justified on the grounds that the jet, although initially supersonic, appears to become unstable and subsonic within the northwest lobe within which it meanders. This also seems to be true of the southeast lobe, provided that one interprets the sinuous bright feature toward the edge of the lobe as part of the counterjet. The forward momentum of both jets therefore seems to have been largely dissipated. On the other hand, the northwest lobe is slightly elongated in the direction of the jet, possibly indicating some residual forward momentum. However, the elongation could also be due to the interaction with the optical line-emitting filaments which we discuss further below. The major part of the southeast lobe seems to be almost spherical, so that this model may be most pertinent to that region of the source. Nevertheless, the derived expansion velocities should be relevant to both lobes, at least to within factors of order unity.

If we assume that the jet energy flux is almost entirely thermalized and the bubble expands adiabatically, then the rate of change of the internal energy, E_L, of each bubble satisfies

$$\frac{dE_L}{dt} = F_E - p\frac{dV}{dt} \ , \quad (6.1)$$

where F_E is the jet energy flux, $V = 4\pi R^3/3$ is the lobe volume, R is its radius, and $p = E_L/(3V)$ is its pressure. We neglect the magnetic pressure. The advance of the lobe into the ISM is preceded by a strong shock. Weaver et al. (1977) modeled this region using a similarity solution. We approximate the region as one of constant density and pressure, the strong shock approximation implying that the lobe pressure and expansion velocity are related by $p = (4/3)\rho_{\rm ISM}(dR/dt)^2$, where $\rho_{\rm ISM}$ is the ambient ISM density. Compared to the Weaver et al. (1977) solution, this approximation is reasonable: their pressure and velocity vary by approximately 20% in this region, and their density varies by less than a factor of 2 before it drops precipitously, marking the edge of the contact discontinuity between bubble and swept-up ISM.

A strong shock is a good approximation in the initial phase of evolution of the bubble, but near the end of the lobe's rapid expansion phase the pressure will come into near-equilibrium with the ISM.

From equation (6.1) above, the radius, expansion velocity, and pressure of the lobe are asymptotically given as functions of time t by

$$R = At^{3/5} \ , \quad (6.2)$$

$$v_{\rm exp} = \frac{3}{5}\frac{R}{t} = 0.6At^{-2/5} \ , \quad (6.3)$$

$$p = \frac{12}{25}\rho_a \frac{R^2}{t^2} = \frac{12}{25}\left(\frac{\mu m_p p_a}{kT}\right)\frac{R^2}{t^2} = \frac{12}{25}\rho_a A^2 t^{-4/5} \ , \quad (6.4)$$

where

$$A = \left(\frac{125F_E}{384\pi\rho_a}\right)^{1/5} = 4.25 \times 10^{13} \ {\rm cm \ s^{-3/5}} \left(\frac{F_{E,44}\,T_7}{p_{\rm ISM,-10}}\right)^{1/5} \ , \quad (6.5)$$

$F_{E,44}$ is the energy flux in units of 10^{44} ergs s^{-1}, $p_{\rm ISM,-10}$ is the ISM pressure in units of 10^{-10} dyn cm^{-2}, and T_7 is the ISM temperature in units of 10^7 K. In terms of M87 parameters,

$$R = 1.7 \text{ kpc} \left(\frac{F_{E,44}\, T_7}{p_{\rm ISM,-10}}\right)^{0.2} t_6^{3/5}, \tag{6.6}$$

$$v_{\rm exp} = 580 \text{ km s}^{-1} \left(\frac{R_{\rm kpc}}{t_6}\right), \tag{6.7}$$

$$\frac{p}{p_{\rm ISM}} = 3.4 T_7^{-1} \left(\frac{R_{\rm kpc}}{t_6}\right)^2, \tag{6.8}$$

where t_6 is the age of the lobe in units of 10^6 yr. Turland (1975) estimated $t_6 \approx 1$ on the basis of the break in the spectrum at 1 GHz. Let us estimate the jet energy flux,

$$F_E = 4\pi c p R_{\rm jet}^2 \left(1 + \frac{\gamma - 1}{\gamma} \mathscr{R}_{\rm jet}\right) \gamma^2 \beta \tag{6.9}$$

(where $\mathscr{R}_{\rm jet} = \rho c^2/4p$ is the ratio of rest-mass energy density to enthalpy for the jet), just upstream of knot A, so that $F_{E,44} = 0.14 p_{-9}[1 + (1 - \gamma^{-1})\mathscr{R}]\gamma^2\beta$. If $p_{-9} = 1$ and $\gamma = 3$, $F_{E,44} = 1.4$; if $\gamma = 5$, $F_{E,44} = 3.4$. For $F_{E,44} \approx 1$, $T_7 \approx 2$, $p_{\rm ISM,-10} = 5$, and $t_6 \approx 1$, the estimated radius of the bubble is approximately 1.4 kpc compared to an observed value of approximately 1.2–1.3 kpc. If $F_{E,44} = 3$, the estimated radius increases to approximately 1.8 kpc. This level of agreement between estimated and observed radii is quite reasonable considering the complications not taken into account in the model: for example, observations suggest that the ambient pressure is not uniform but varies by about a factor of 2. Moreover, the 12″ VLA images of Böhringer et al. (1995) indicate that a significant fraction of the radio plasma is "leaking" from the inner lobes, so that not all of the jet energy flux is available to power expansion. On the other hand, the morphology of the 0.″4 image of Hines et al. (1989) suggests that the jet energy flux is not all that much larger than our estimates. This is one of the reasons we favor $\gamma \lesssim 5$ for the bulk Lorentz factor of the jet.

In estimating the expansion velocity and the pressure, we insert the observed radius into equations (6.7) and (6.8), thus avoiding any uncertainty associated with the energy flux. The calculated expansion velocity is approximately 750 km s^{-1}. The ratio of lobe pressure to ISM pressure is ≈ 3 so that the interior pressure in the bubble is approximately 1.5×10^{-9} dyn cm^{-2}, consistent with the estimates of minimum pressures discussed in § 2 and (to within a factor of 2) with the estimates in § 3 based upon shock pressure ratios and the pressure of knot A. (One should not, of course, expect better than "factor of order unity" agreement among the different estimates of the pressure, in view of our neglect of the magnetic field in treating jet shocks and our reliance on estimates of minimum pressures.)

The calculated pressure ratio shows that the assumption of a strong shock preceding the lobe is only marginally consistent, although this would not have been the case during the past history of the lobe. What these calculations do appear to show is that the expansion of the lobe is starting to stall as it comes into equilibrium with the interstellar medium. Nevertheless, a present expansion velocity for the lobe of the order of 750 km s^{-1} seems quite reasonable.

An important implication of the dynamics of a transiently overpressured jet driving the expansion of a lobe which itself it overpressured with respect to the ambient medium is that it is not necessary to invoke a magnetic field in order to confine the jet.

6.2. *The Optical Line-emitting Filaments*

6.2.1. *Energy Budget*

The expansion of the M87 lobes provides an obvious source of input power for the optical line-emitting filaments adjacent to the radio lobes. The excitation of these filaments has been a long-standing problem ever since Ford & Butcher (1979) showed that other potential sources of excitation such as the UV flux from the jet fail to provide sufficient ionizing photons. In our picture, the optical emission-line luminosity is powered by the interaction between the expanding shell surrounding the radio lobe and cool dense clouds in the M87 cooling flow. Morphological support for this idea stems from the fact that although some parts of the filaments are seen in projection against the lobes, other regions are offset from the lobes. The visual impression from the radio-optical image of Sparks et al. (1993) is that the filaments appear to be wrapped *around* the lobes. The input of energy to the dense gas could occur through internal radiative (possibly autoionizing) shocks induced by the impact of the shocked ISM external to the expanding lobes upon cool gas clouds in the inner regions of the cooling flow. The first detailed analysis of autoionizing shocks by Binette et al. (1985) was, in fact, directed toward understanding the spectra of the M87 filaments. More recently, as mentioned in § 2, the data on the M87 emission-line disk have been modeled by M. Dopita (1995, private communication) using a shock velocity of 200 km s^{-1}. Since such shocks are strongly radiative, their luminosity is indicative of the energy flux incident upon them. Therefore, in order for this idea to be viable, the hydrodynamic energy flux associated with the expansion of the bubble should comfortably exceed the total line luminosity.

The energy flux of the ISM being pushed outward by the expanding bubble in a more or less spherical piston flow and intercepting the filaments is

$$\begin{aligned} F_{E,\rm ISM} &= \frac{5}{2} p v_{\rm exp} A \left(1 + \frac{M^2}{3}\right) \\ &= 1.0 \times 10^{43} \text{ ergs s}^{-1} \\ &\quad \times \left(\frac{p}{5 \times 10^{-10}}\right)\left(\frac{A}{8.4 \times 10^6 \text{ pc}^2}\right) \\ &\quad \times \left(\frac{v_{\rm exp}}{10^3 \text{ km s}^{-1}}\right)\left(1 + \frac{M^2}{3}\right), \end{aligned} \tag{6.10}$$

where A is the area of the intercepted flow and the fiducial value of 8.4×10^6 pc^2 is the projected area of the filaments. The parameter M is the Mach number of the ISM driven out by the lobe.

The Hα luminosity of the filaments is $\approx 8.3 \times 10^{39}$ ergs s^{-1} (Sparks et al. 1993), implying a total emission-line luminosity some 100 times greater, i.e., $\sim 10^{42}$ ergs s^{-1}. Thus, for the typical expansion velocities and Mach numbers we

have inferred for the expanding lobe, the conversion of mechanical energy to emission-line luminosity is only required to be of order 10% efficient.

6.2.2. *Emission-Line Excitation*

Having established an energy budget for the emission-line filaments, let us now consider in detail how the emission-line filaments would be produced. We first note that condensations in the M87 cooling flow are likely, since the cooling timescale in the ISM is $t_c \approx 2.5 \times 10^7\ T_{\rm ISM,7}^2\, p_{\rm ISM,-9}^{-1}\, \Lambda_{-23}^{-1}$ yr, where $T_{\rm ISM,7}$ is the ISM temperature in units of 10^7 K, $p_{\rm ISM,-9}$ is the ISM pressure in units of 10^{-9} dyn cm^{-2}, and $\Lambda_{-23}(T)$ is the cooling function in units of 10^{-23} ergs cm^3 s^{-1}. Thus, on a timescale of 10^7–10^8 yr, gas will cool in the inner regions of M87 where $p_{-9} \approx 0.5$, $T_7 \approx 2$ and $\Lambda_{-23} \approx 3$. Indeed, Böhringer et al. (1995) have discovered evidence for cooling gas outside a few kiloparsecs from the center. Moreover, the cooling timescale decreases toward the inner few kiloparsecs, since the pressure increases with decreasing radius. Qualitatively, therefore, it is likely that there will be a buildup of cooling gas toward the radio lobes.

As noted in § 2, emission-line modeling indicates that the shock velocities required to fit the spectrum of the filaments are $\sim$200 km s^{-1}. Assuming that these filaments are high-density, low-temperature clouds swept up by the shell of gas just outside the expanding bubble, we can estimate their density as follows. We assume parameters for the bubble shell consistent with those derived above, i.e., a pressure ratio (compared to the ISM) of 3, with a corresponding pressure, $p_{\rm shell} \approx 1.5 \times 10^{-9}$ dyn cm^{-2}. This implies a density jump (from ISM to shell) of approximately 1.9. In the frame of the cloud the shell is mildly supersonic, so that when this impinges on the cloud a mild bow shock forms, producing a stagnation pressure adjacent to the cloud $\approx p_{\rm shell} + \rho_{\rm shell} v_{\rm exp}^2$, where $\rho_{\rm shell}$ is the density of swept-up hot ISM in the shell. (This reasonably assumes that the bow shock is adiabatic.) Taking $\rho_{\rm shell} = 3.6 \times 10^{-25}$ g cm^{-3} and $v_{\rm exp} = 750$ km s^{-1} gives a stagnation pressure $p_{\rm st} \approx 3.5 \times 10^{-9}$ dyn cm^{-2}. This pressure drives a shock into the cloud with a velocity

$$v_{\rm shock} \approx \left(\frac{3}{4}\right)^{1/2} \left(\frac{p_{\rm st}}{\mu m_p n_{\rm cl}}\right)^{1/2}, \qquad (6.11)$$

where $n_{\rm cl}$ is the number density of the cloud. Inverting this equation gives a cloud number density $n_{\rm cl} \approx 7$ cm^{-3} $(p_{\rm st}/3.5 \times 10^{-9}$ dyn cm$^{-2})(v_{\rm shock}/200$ km s$^{-1})^{-2}$.

The subsequent evolution of the gas following the radiative shock in the cloud depends upon the strength of the magnetic field. If there were no field, the gas would cool to a temperature $\sim 10^4$ K from an immediate postshock temperature, $T_{\rm ps} \approx (3/16)\mu m_p v_{\rm shock}^2 = 3.2 \times 10^5$ K. The density in the recombination zone would therefore be approximately a factor of 30 higher than the immediate postshock density and would certainly not be in the low-density limit implied by the observations. This indicates that magnetic field is important in preventing the collapse of the postshock plasma to a high density (see § 2 and Dopita & Sutherland 1996a).

Making the usual assumption of isobaric conditions behind the shock, the magnetic pressure in the recombination zone is roughly equal to $p_{\rm st}$. Assuming that the postshock field is primarily transverse to the flow and therefore proportional to the density, the density in the recombination zone is given by

$$n_{\rm recom} = \frac{(8\pi)^{1/2} p_{\rm st}^{1/2}}{B_{\rm cl}}\, n_{\rm cl} = \frac{3}{4} \frac{(8\pi)^{1/2} p_{\rm st}^{3/2}}{B_{\rm cl}\, \mu m_p\, v_{\rm shock}^2}, \qquad (6.12)$$

where $B_{\rm cl}$ is the magnetic flux density in the unshocked cloud and the second form of this equation follows from equation (6.11) relating the shock velocity and cloud density. Numerically,

$$n_{\rm recom} \approx 190\ {\rm cm}^{-3} \left(\frac{p_{\rm st}}{3.5 \times 10^{-9}\ {\rm dyn\ cm}^{-2}}\right)^{3/2} \times \left(\frac{v_{\rm shock}}{200\ {\rm km\ s}^{-1}}\right)^{-2} \left(\frac{B_{\rm cl}}{10\ \mu{\rm G}}\right)^{-1}. \qquad (6.13)$$

Owen et al. (1990) have estimated the strength of the magnetic field in a 0.3–1 kpc "shell" around each radio lobe to be between 20 and 40 μG on the basis of Faraday rotation measurements. Clearly, assuming that a magnetic field of this order of magnitude permeates the filaments, and that the shock velocity is of order 200 km s^{-1}, the electron density within the recombination zone is within the low-density limit ($\sim$100 cm^{-3}) implied by the [S II] ratio. Dopita's shock modeling (see § 2) provides further *independent* evidence that the magnetic field in the filaments is strong enough to prevent overdense regions from occurring.[4] If the magnetic parameter is of the same order of magnitude as required for his modeling of the disk spectrum (8 μG cm$^{3/2}$), then a magnetic field $\sim$20–40 μG is also indicated.

Clouds with an initial number density $\sim$10 cm^{-3} cannot be in pressure equilibrium with the ISM of M87. For pressure equilibrium at a density of 10 cm^{-3}, a temperature of $\approx 2 \times 10^6$ K is required. Gas at this temperature is thermally very unstable and, more important, could not be the source of the observed emission lines. Rather, 2×10^6 K must represent the temperature at which clouds, condensing out of the ISM, can no longer remain isobaric; the real temperature of the clouds must be considerably smaller ($\lesssim 10^4$ K). The minimum size for the condensing clouds, $l_{\rm min}$, is given by the condition that the sound crossing time be comparable to the cooling time, implying

$$l_{\rm min} \approx 12 p_{-9}\, T_7^{5/2}\, \Lambda_{-23}^{-1}\ {\rm kpc} = 200 \Lambda_{-23}^{-1}\ {\rm pc} \qquad (6.14)$$

for $T_7 = 0.2$ and $p_{-9} = 0.5$. Hence the minimum size for the clouds is of order 100 pc. The contour map of Sparks et al. (1993) shows that the observed transverse size of the filaments is a factor of a few larger than this.

As clouds condense out of the ISM, they would be subject to shocks driven into them by the ISM itself. These would have a somewhat lower velocity ($\approx$90 km s^{-1}) than the shocks originating from interaction with the shell. For clouds near the present location of the bubble, the shock crossing time for a cloud of the minimum size is of order 10^6 yr, that is, of the order of the age of the radio bubble. This

[4] Shock models constrain the magnetic field by virtue of the fact that the magnetic field prevents the recombination zone from becoming too dense and thereby prevents low-ionization lines from becoming too strong in the spectrum.

coincidence is significant, since it means that the filaments will not have been traversed completely by the weaker ISM-driven shocks before they interact with the expanding shell. It is also possible that the clouds that are intercepted by the expanding shell are those that have just formed in the external cooling flow.

The observed velocities of the filaments are consistent with this theory. As noted in § 2, Sparks et al. (1993) discovered that the filaments associated with the northwest radio lobe are blueshifted by about 100 km s^{-1} and also argued that they are in front of the radio lobes. On the basis of our model the postshock velocity should be $(3/4)v_{\rm shock} \approx 150$ km s^{-1}.

Another interesting feature of this theory is that for filament sizes greater than 100 pc the shocks will not have completely traversed the filaments, which could therefore contain a significant amount of neutral material. This may explain the anomalous dust-to-gas ratio for the M87 filaments inferred by Sparks et al. (1993). It is also of interest to note that the size of the Faraday screen detected by Owen et al. (1990) is ~0.3–1 kpc. This is of the order of the size of the compressed shell surrounding the radio lobes implied by our bubble model. It is therefore feasible that this shell contains interstellar magnetic field compressed by the shock preceding the radio lobe.

7. INITIAL EXPANSION OF THE JET AND DENSITY WITHIN THE RADIO LOBES

7.1. *The Initial Region of Constant Cone-Angle Expansion*

So far we have not considered the region of initial transverse expansion of the jet before it reaches the prominent knots. However, it is important to relate this to the physics proposed in the previous sections.

It has often been suggested that the region of the jet out to knot A represents a regime of free expansion. This notion is inconsistent with the physics of the previous sections, since a free jet would not interact with the surrounding medium in the manner we have proposed, to produce oblique shocks. Nevertheless, it is of interest to estimate the Lorentz factor implied by free expansion. For a freely expanding jet, the Mach number is related to the expansion angle by $M \approx 2/\theta_{\rm exp}$. The intrinsic expansion angle is smaller than the observed angle by a factor $\sin\theta$, where, as before, θ is the angle between the jet axis and the observer. Since the observed expansion angle is 6°.5 the minimum Mach number is 18 (for $\theta = 90°$); for $\theta = 30°$ the Mach number would be 36. The Mach number for relativistic flow is $\gamma_v v/(\gamma_{c_s} c_s) = 2^{1/2}\gamma\beta$ for $\mathscr{R}_j = 0$, where c_s is the sound speed (Königl 1980); the minimum Lorentz factor therefore is approximately 13, and if $\theta = 30°$, $\gamma = 25$. The jet energy flux implied by such values is 1–2 orders of magnitude higher than what we have considered previously and Lorentz factors this high can be discounted for this reason alone. Moreover, these Lorentz factors are also comparable to or exceed estimates for most quasars.

A qualitatively different explanation for the initial conical expansion of the jet is that it is due to the injection of mass from stars along its path through the normal processes of stellar mass loss via winds (Phinney 1983; Komissarov 1994). Following Komissarov (1994), such an entrainment process can be represented by the following jet equations:

$$\frac{d}{dz}(w\gamma uA) = \dot{\rho}cA\,, \tag{7.1}$$

$$\frac{d}{dz}(wu^2A) = -A\frac{dP}{dz}\,, \tag{7.2}$$

$$\frac{d}{dz}(\rho c^2 uA) = \dot{\rho}cA\,, \tag{7.3}$$

where $u = \gamma\beta$ is the proper velocity (in units of c), $w = \rho c^2 + 4p$ is the relativistic enthalpy, z is the distance along the jet, A is the jet cross-sectional area, and it is assumed that the jet is confined, so that p is the pressure of the ambient medium. The quantity $\dot{\rho}$ is the rate of change of density in the jet as a result of mass injection by stars.

The rate of change of the 4-velocity can be determined from the above equations to be

$$\frac{du}{dz} = -\gamma\frac{\dot{\rho}c}{w} - \frac{\gamma^2}{wu}\frac{dp}{dz}\,, \tag{7.4}$$

so that a convenient parameter for this mode of entrainment is

$$\chi = \frac{\dot{\rho}_0 c z_0}{w_0}\,, \tag{7.5}$$

where $\dot{\rho}_0$ is the central rate of density increase, w_0 is the jet (relativistic) enthalpy at an appropriate initial point, and z_0 is an appropriate scale length. The parameter χ represents the relative change of jet density in the time that it takes an element of the jet to travel a distance z_0. Numerically

$$\chi = 0.98\left(\frac{\dot{M}_w}{10^{-12}\ M_\odot\ {\rm yr}^{-1}\ M_\odot^{-1}}\right)\left(\frac{\rho_{*,0}}{20\ M_\odot\ {\rm pc}^{-3}}\frac{z_0}{\rm kpc}\right) \times\left(\frac{p_0}{10^{-9}\ {\rm dyn\ cm}^{-2}}\right)^{-1}(1+\mathscr{R}_{j,0})^{-1}\,, \tag{7.6}$$

where $\dot{M}_w$ is the rate of mass injection per solar mass due to stellar winds, $\rho_{*,0}$ is the central stellar mass density whose value for M87 is $20\ M_\odot\ {\rm pc}^{-3}$ (Sargent et al. 1978), and $\mathscr{R}_{j,0}$ is the initial value of $\mathscr{R}_j$.

The fact that $\chi \sim 1$ indicates that this mode of entrainment should be taken seriously in this case. However, there are a number of factors to be taken into account: (1) whether the injected mass is mixed into the jet plasma, effectively loading the jet; (2) whether an effective spreading rate as observed can be reconciled with the maintenance of the jet velocity at a relativistic value; (3) the effects of pressure gradients within the bubble. Thus a detailed study of this process is not undertaken here. We merely comment that it *may* be important.

The morphology of the M87 jet does not seem to be consistent with turbulent entrainment, since there is no evidence for large-scale eddies or filamentary structure that could be responsible for the engulfing of mass from the surrounding medium. However, another possibility for the initial expansion is that it is a result of internal dissipation leading to a self-similar type of flow.

7.2. *Contribution of Stellar Mass Loss to the Internal Density of the Bubbles*

Whether or not mass injection by stars is responsible for the initial expansion of the jet, this process appears to be

relevant to the cold matter density in the interior of the expanding radio lobes. The mean mass density[5] at time t in an expanding lobe is

$$\bar{\rho}_{\rm lobe}(t) = V(t)^{-1} \int \left[\int_{\rm lobe} \rho_* \dot{M}_w \, dV(t') \right] dt' . \quad (7.7)$$

It is straightforward to evaluate this expression for a uniform stellar mass density. However, the core radius of the stellar distribution, $r_c = 9''.6 = 790$ pc, is small compared to the diameters of the radio lobes, $\approx 30''$, hence a more accurate calculation is required. In keeping with the approximations of the previous sections, we have adopted the King approximation for the stellar mass distribution, $\rho_* = \rho_{*,0}(1 + r^2/r_c^2)^{-3/2}$, and we have approximated the lobes as expanding spheres with the end of one diameter at the center of the galaxy. The result of the calculation is that after 10^6 yr, when the radius of the lobe is 1.2 kpc, the mean density within the lobe is 1.1×10^{-28} g cm^{-2} corresponding to a particle density $\approx 7 \times 10^{-5}$ cm^{-3} and total mass inside the lobe of $\approx 10^4 \, M_\odot$. The corresponding value of $\mathcal{R}_a = \bar{\rho} c^2 / 4p \approx 25 p_{-9}^{-1}$ is on the small side (especially for $p_{-9} \approx 2$) but is within an order of magnitude of the value ~ 100 indicated by the analysis of the Kelvin-Helmholtz instability in § 4.

Thus, mass injection by stars is a significant contributor to the thermal matter inside the radio lobes. We do not expect the hot ISM outside the lobes to contribute much mass, since the decelerating interface between the radio lobe and the hot ISM is Rayleigh-Taylor stable. However, it is possible that the filamentary dense emission-line gas will contaminate the bubble, since the shocks impart a velocity to it of ~ 200 km s^{-1} and we have estimated that the bubble is moving outward at ~ 750 km s^{-1}. Sparks et al. (1993) estimate the mass of the filaments (if completely ionized) to be $\sim 5 \times 10^5 \zeta^{-1} \, M_\odot$, where ζ is the overpressure ratio with respect to the hot ISM. We estimate $\zeta \approx 3$ from equation (6.8), so that the filamentary mass $M_{\rm fil} \sim 2 \times 10^5 \, M_\odot$ and the lobe pressure $p_{\rm lobe} \approx 1.5 \times 10^{-9}$ dyn cm^{-2}. If a mass comparable to this has already been swept up by the expanding lobes, then this would dominate the mass injected by stars. This would also give a value of $\mathcal{R}_a \sim 400$—slightly higher than we have estimated from the Kelvin-Helmholtz analysis, but not excessively so.

A process which could impede the incorporation of the shocked filament material into the expanding radio lobe is the subsequent shredding of the shocked clouds by the Kelvin-Helmholtz instability (Klein, McKee, & Colella 1994). The resulting small clouds could be swept outward by ram pressure of the expanding shell and not penetrate the bubble at all. However, the shredding takes place on several cloud crushing timescales, i.e., $\sim 10^6$ yr—comparable to the age of the lobes. Therefore, it is probably inevitable that a significant fraction of the dense clouds penetrates the radio lobes.

8. DISCUSSION AND CONCLUSIONS

In this paper, motivated principally by the proper-motion data on the M87 jet assembled by Biretta et al. (1995) from a decade of observations, we have proposed a reasonably consistent picture of the inner kiloparsec of M87 which links the physics of shocks and instabilities in relativistic jets, the evolution of the kiloparsec-scale radio lobes, and the excitation of the optical line-emitting filaments.

By applying the kinematics of relativistic shocks to knot A, we have shown that this knot, contrary to its appearance on the sky, is probably an oblique shock and that the most likely angle between the jet plasma velocity and the shock normal is within about 10° of the Mach angle. This is an appealing deduction, since one expects shocks in supersonic jets to be near the Mach angle if they are not to be immediately disruptive.

For a relativistic jet with a moderate Lorentz factor, the pressure jump of ~ 5 at knot A can be reconciled with the observed small deflection angle of $\sim 5°$–$6°$. The other knots in the jet also appear to us to be oblique shocks, as do the faint striations observed all along the jet (which give the impression of helical filaments wound around the jet). Similar physics to that proposed for knot A would be pertinent to these structures as well. However, the fortunate circumstance that knot A appears to be edge on provides an important constraint on its parameters, specifically on its obliquity and the normal component of its velocity.

We have investigated a plausible mechanism which may be responsible for oblique shocks in the M87 jet in particular, and in relativistic jets in general: the helical ($m = 1$) Kelvin-Helmholtz instability. The twisting of the jet resulting from this instability leads to the production of shocks due to the bending of the supersonic flow. The obvious large-amplitude bending of the jet beyond knot A makes this an appealing mechanism, and the parameters necessary in order for it to be viable lead to some interesting constraints on jet and radio lobe parameters. In order to produce the observed wavelength of the jet oscillations and the velocities of the knots by this mechanism, the medium surrounding the jet must be of the order of 10–100 times denser than the jet plasma itself. While the radio lobe is much denser than the jet, it is much less dense than the interstellar medium, implying that the radio lobes are forming low-density, high-pressure bubbles in the central 5 kpc of M87. We have shown in § 7 that the inferred density of thermal material in the radio lobes could be supplied by a combination of stellar mass loss during the lifetime of the lobes together with the sweeping up of clouds that have condensed out of the ISM. The exact contribution of the latter is somewhat problematical, of course, since we do not know the distribution of clouds before the formation of the radio lobes.

The proposal that the jet knot pressures are transient overpressures resulting from shocks and that the lobes themselves are overpressured with respect to the ambient medium imply that it is no longer necessary to invoke magnetic field for the confinement of the jet.

The inference that the radio lobes are expanding at ~ 750 km s^{-1} into the surrounding medium has interesting implications for the emission-line structure surrounding the lobes. As we remarked in § 2, there are good reasons to believe that this gas excited by 200 km s^{-1} radiative shocks. In order to obtain the required shock speed, we require these clouds to be underpressured with respect to the background cooling flow outside the bubble. This occurs if the clouds are sufficiently large (> 100 pc across) that when they form in the cooling flow, they lose pressure contact with the surrounding ISM and cool isochorically. Such clouds could

[5] It is appropriate to calculate a mean density, since the thermal matter within the lobes will be redistributed by the swirling jet flow within the lobe.

have formed through recent ($\lesssim 10^6$ yr ago) thermal instabilities.

We suggest that, in the case of the M87 filaments, the production of shocks occurs when the cool gas is intercepted by the shocked ISM preceding the expanding lobe, and we have shown that the inferred energy flux associated with the expansion of the lobe can comfortably account for the observed emission-line flux. Our proposed mechanism for the excitation of emission lines in M87 provides another example of an active galaxy in which mechanical energy input mediated by shocks may be important in determining the emission-line luminosity (see Sutherland, Bicknell, & Dopita 1993 and Dopita & Sutherland 1996a, 1996b).

In § 5 we have indicated that synchrotron cooling in an inhomogeneous magnetic field may be responsible for the optical to X-ray spectrum of the knots in the M87 jet. More detailed modeling of postshock spectra is required to confirm this. Nevertheless, the fact that good agreement exists between the estimated and observed break frequencies in the jet is circumstantial evidence in favor of this idea. If this basic model is correct, we expect that measurements of optical spectral indices at high spatial resolution should show considerable steepening between the knots.

The initial rate of expansion of the jet has long been an enigma. If the expansion were free, the Mach number and Lorentz factor would be too large to be sensible. One possible solution is that mass injection into the jet by stars, as proposed by Komissarov (1994) and Phinney (1983), significantly contributes to the rate of expansion with some implied deceleration. Another possibility is that dissipation along the length of the jet contributes to the expansion. As our discussion in § 7 shows, these possibilities require further attention. A third possibility is that the jet expands as a result of turbulence triggered by surface entrainment. However, the morphology of the jet does not appear to support this idea.

As far as the parameters of the M87 jet are concerned, consistency among the shock solutions, the Kelvin-Helmholtz instability, the surface brightness ratio of jet to counterjet, and the expansion of the lobes suggests that the Lorentz factor is in the range 3–5 with a fairly low cold matter component ($\mathscr{R}_j \lesssim 2$). The angle to the line of sight is probably around 30°–35°.

We should also comment on the age of the inner lobes ($\sim 10^6$ yr) implied by this model. This is remarkable in view of the much more extended radio halo of M87 observed at low frequency (see Fig. 1 of Biretta & Meisenheimer 1993), whose age, in keeping with the estimates of the ages of most radio galaxies, is likely to be $\sim 10^8$–10^9 yr. Probably, the only sensible way that one can reconcile such disparate numbers is to conclude that the inner lobes are a transient but frequently repeated phenomenon in the center of M87. Cycling of the output of the central black hole could result if mass influx from the cooling flow is followed by choking of the latter due to the formation of the inner lobes, which then dissipate, allowing further inflow and so on. The cycling timescale is essentially the time taken, $\sim 10^6$–10^7 yr, for the inner lobes to come into pressure equilibrium with their surroundings. Binney & Tabor (1995) have advocated a similar model for AGN-related cooling flows in which "short bursts of energy alternate with periods of quiescent cooling."

Finally, we note that, although M87 has obviously been the target of the theory developed here, a substantial amount of the physics may also be applicable to other radio galaxies. Important topics for further study include the formation of shocks via the Kelvin-Helmholtz instability, relativistic effects on the appearance of shocks, the relation between knot and jet velocities, the production of spectral breaks greater than 0.5 in jet spectra, and the production of emission lines through interaction of ambient gas with expanding radio lobes. Indeed, the physics of M87 may well have much in common with the class of VLBI source known as compact symmetric objects (e.g., Conway et al. 1994; Wilkinson et al. 1994). A model for these objects, involving jet-driven bubbles, has been proposed by Begelman (1996), who has shown that the statistics of CSOs may be explained by expansion into an atmosphere whose density is proportional to r^{-2}. This model has been developed further by Bicknell, Dopita, & O'Dea (1996a) (see also Bicknell, Dopita, & O'Dea 1996b), who propose that the turnovers in the radio spectra and the emission-line luminosities of gigahertz peak spectrum radio sources result from the properties of shocks enveloping the expanding lobes.

A large amount of the work for this paper was done while G. V. B. was the recipient of a Visiting Fellowship at JILA, University of Colorado. G. V. B. would like to thank the Chairman and Fellows of JILA for the opportunities afforded by this fellowship and for their hospitality. We are also grateful to M. A. Dopita for discussions on the spectrum of M87 and for a thorough reading of the original manuscript, and to J. Biretta for promptly answering our numerous inquiries concerning the M87 data. M. C. B. gratefully acknowledges partial support through National Science Foundation grant AST 91-20599.

APPENDIX

APPEARANCE OF RELATIVISTICALLY MOVING SHOCKS

The apparent rotation of relativistically moving objects is a well-known effect, and some of the ramifications for VLBI observations have been discussed by Marscher, Gear, & Travis (1991). In this appendix we derive relationships describing the apparent velocity and orientation of a relativistically moving shock in a form which is suitable for the type of calculations we wish to pursue. One of the main results that emerges from this analysis is that apparently edge-on shocks are preferred. We also show how the normal component of the shock velocity can be inferred from the observational data. This information is utilized in the solution of the relativistic Rankine-Hugoniot equations, and procedures for doing this are also described.

A1. BASIC RELATIONS

We establish observer-related (subscript "obs") and jet-related (subscript "jet") coordinate systems, as follows (see Fig. 2):

the z_{obs} axis points toward the observer, and the z_{jet} axis is in the direction of the (three-dimensional) shock pattern speed and makes an angle θ with the z_{obs} axis. The x_{obs} axis lies in the intersection of the plane of the sky with the plane defined by $z_{obs} - z_{jet}$. The y_{obs} and y_{jet} axes are identical and lie in the plane of the sky and are perpendicular to the plane defined by z_{obs} and z_{jet}. The x_{jet} axis completes the orthonormal frame defined by y_{jet} and z_{jet}. The jet frame is *unboosted* with respect to the observer frame but is related to it by a rotation, through the angle θ, i.e.,

$$\begin{pmatrix} x_{jet} \\ y_{jet} \\ z_{jet} \end{pmatrix} = \begin{pmatrix} \cos\theta & 0 & -\sin\theta \\ 0 & 1 & 0 \\ \sin\theta & 0 & \cos\theta \end{pmatrix} \begin{pmatrix} x_{obs} \\ y_{obs} \\ z_{obs} \end{pmatrix} . \tag{A1}$$

Now consider a planar shock (or a section of a shock which can be considered to be locally plane). The shock propagates with a three-dimensional velocity $\beta_p \boldsymbol{k}_{jet}$, where $\boldsymbol{k}_{jet}$ is the unit vector in the z_{jet} direction; we define the unit normal to the shock plane in the jet frame to be $\boldsymbol{n}_{jet} = (n_{x,jet}, n_{y,jet}, n_{z,jet})$. In § 3 we describe $\boldsymbol{n}$ in terms of polar angles ψ and ϕ defined by

$$n_x = \sin\psi \cos\phi , \qquad n_y = \sin\psi \sin\phi , \qquad n_z = \cos\psi . \tag{A2}$$

Thus, at time t_{jet} the location of the shock front is

$$\boldsymbol{r}(t_{jet}) = \boldsymbol{r}_0 + \beta_p t_{jet} \boldsymbol{k}_{jet} , \tag{A3}$$

where $\boldsymbol{r}_0 = (x_{0,jet}, y_{0,jet}, z_{0,jet})$ represents the shock plane at $t_{jet} = 0$. The origin of time is chosen so that the shock intersects $\boldsymbol{r} = 0$ at $t_{jet} = 0$. Consequently, $\boldsymbol{n} \cdot \boldsymbol{r}_0 = 0$.

In calculating the observed orientation of the shock, one must take into account not only the purely geometrical effect of the rotation of the reference frame, but also the fact that photons arriving simultaneously at the observer are emitted from the shock front at different times. That is, one must allow for the effect of time retardation. [It is time retardation that gives the well-known result (Rees 1966) that the apparent speed of a feature in a jet is $\beta_a = \beta \sin\theta/(1 - \beta\cos\theta)$, where β is the actual speed.]

A ray emitted from a point $\boldsymbol{r}_{jet}(t_{jet})$ on the shock surface is recorded by the observer at a time

$$t_{obs} = t_{jet} - z_{obs}(t_{jet}) , \tag{A4}$$

where $t_{obs} = 0$ corresponds to the arrival of the ray from $(\boldsymbol{r}_{jet}, t_{jet}) = 0$ and units are such that $c = 1$. Equivalently, for a given observer time t_{obs}, equation (A4) defines the time t_{jet} at which a given ray is emitted.

Taking time retardation into account, the locus of points on the apparent shock front is given by

$$\begin{aligned} x_{obs} &= x_{0,obs} + (\beta_p \sin\theta) t_{jet} = x_{0,obs} + (\beta_p \sin\theta)(t_{obs} + z_{obs}) , \\ y_{obs} &= y_{0,obs} , \\ z_{obs} &= z_{0,obs} + (\beta_p \cos\theta) t_{jet} = z_{0,obs} + (\beta_p \cos\theta)(t_{obs} + z_{obs}) , \end{aligned} \tag{A5}$$

where $x_{0,obs}$, $y_{0,obs}$, and $z_{0,pbs}$ are simply given by the rotation of the coordinate system, viz.,

$$\begin{pmatrix} x_{0,obs} \\ y_{0,obs} \\ z_{0,obs} \end{pmatrix} = \begin{pmatrix} \cos\theta & 0 & \sin\theta \\ 0 & 1 & 0 \\ -\sin\theta & 0 & \cos\theta \end{pmatrix} \begin{pmatrix} x_{0,jet} \\ y_{0,jet} \\ z_{0,jet} \end{pmatrix} . \tag{A6}$$

Equation (A5) for z_{obs} is easily solved to give

$$z_{obs} = \frac{z_{0,obs}}{1 - \beta_p \cos\theta} + \left(\frac{\beta_p \cos\theta}{1 - \beta_p \cos\theta} \right) t_{obs} , \tag{A7}$$

implying that

$$x_{obs} = \left(x_{0,obs} + \frac{\beta_p \sin\theta}{1 - \beta_p \cos\theta} z_{0,obs} \right) + \left(\frac{\beta_p \sin\theta}{1 - \beta_p \cos\theta} \right) t_{obs} , \tag{A8}$$

and giving the (expected) transverse proper motion

$$\beta_a = \frac{\beta_p \sin\theta}{1 - \beta_p \cos\theta} , \tag{A9}$$

implying that

$$\beta_p = \frac{\beta_a}{\sin\theta + \beta_a \cos\theta} . \tag{A10}$$

Since $\boldsymbol{n}$ is perpendicular to the shock front, then

$$n_{x,obs} x_{0,obs} + n_{y,obs} y_{0,obs} + n_{z,obs} z_{0,obs} = 0 , \tag{A11}$$

where the components of $\boldsymbol{n}$ in this equation are rotated to the observer's reference frame. Solving equations (A7) and (A8) for $x_{0,\mathrm{obs}}$ and $z_{0,\mathrm{obs}}$ and substituting in equation (A11) implies

$$n_{x,\mathrm{obs}}[x - (\beta_p \sin\theta)z - \beta_p t \sin\theta] + n_{y,\mathrm{obs}}\, y + n_{z,\mathrm{obs}}[(1 - \beta_p \cos\theta)z - \beta_p t \cos\theta] = 0\,. \tag{A12}$$

The gradient of the left-hand side of this equation gives the (nonunit) normal to this surface as

$$\begin{pmatrix} m_{x,\mathrm{obs}} \\ m_{y,\mathrm{obs}} \\ m_{z,\mathrm{obs}} \end{pmatrix} = \begin{pmatrix} n_{x,\mathrm{obs}} \\ n_{y,\mathrm{obs}} \\ n_{z,\mathrm{obs}} - \beta_p[(\cos\theta)n_{z,\mathrm{obs}} + (\sin\theta)n_{x,\mathrm{obs}}] \end{pmatrix} = \begin{pmatrix} n_{x,\mathrm{obs}} \\ n_{y,\mathrm{obs}} \\ n_{z,\mathrm{obs}} - \beta_p n_{z,\mathrm{jet}} \end{pmatrix}. \tag{A13}$$

In coordinate invariant form,

$$\boldsymbol{m} = \boldsymbol{n} - \beta_n \boldsymbol{k}_{\mathrm{obs}}\,, \tag{A14}$$

where $\boldsymbol{k}_{\mathrm{obs}}$ is the unit vector in the direction of the observer and $\beta_n = \beta_p n_{z,\mathrm{jet}}$ is the component of the shock velocity along the shock normal. The vector $\boldsymbol{m}$ points in the direction of the *apparent* shock normal. The inverse of equation (A13) is

$$\begin{pmatrix} n_{x,\mathrm{obs}} \\ n_{y,\mathrm{obs}} \\ n_{z,\mathrm{obs}} \end{pmatrix} = \begin{pmatrix} m_{x,\mathrm{obs}} \\ m_{y,\mathrm{obs}} \\ [m_{z,\mathrm{obs}} + (\beta_p \sin\theta)m_{x,\mathrm{obs}}]/(1 - \beta_p \cos\theta) \end{pmatrix}. \tag{A15}$$

Other useful relations in transforming between components of $\boldsymbol{m}$ and $\boldsymbol{n}$ in the two reference frames are

$$\begin{pmatrix} m_{x,\mathrm{obs}} \\ m_{y,\mathrm{obs}} \\ m_{z,\mathrm{obs}} \end{pmatrix} = \begin{pmatrix} \cos\theta & 0 & \sin\theta \\ 0 & 1 & 0 \\ -\sin\theta & 0 & \cos\theta - \beta_p \end{pmatrix} \begin{pmatrix} n_{x,\mathrm{jet}} \\ n_{y,\mathrm{jet}} \\ n_{z,\mathrm{jet}} \end{pmatrix} \tag{A16}$$

and the inverse,

$$\begin{pmatrix} n_{x,\mathrm{jet}} \\ n_{y,\mathrm{jet}} \\ n_{z,\mathrm{jet}} \end{pmatrix} = \begin{pmatrix} (\cos\theta - \beta_p)/(1 - \beta_p \cos\theta) & 0 & -\sin\theta/(1 - \beta_p \cos\theta) \\ 0 & 1 & 0 \\ \sin\theta/(1 - \beta_p \cos\theta) & 0 & \cos\theta/(1 - \beta_p \cos\theta) \end{pmatrix} \begin{pmatrix} m_{x,\mathrm{obs}} \\ m_{y,\mathrm{obs}} \\ m_{z,\mathrm{obs}} \end{pmatrix}. \tag{A17}$$

A2. RELATIONSHIP BETWEEN APPARENT SHOCK DIRECTION AND DIRECTION IN THE JET FRAME

Using the above formulae, it is straightforward to establish relationships between observed angles of the apparent shock front and the intrinsic angles in the jet frame.

The fact that $\boldsymbol{n}$ is a unit vector implies that the components of $\boldsymbol{m}$ satisfy (see eq. [A15])

$$m_x^2 + m_y^2 + \frac{[m_z + (\beta_p \sin\theta)m_x]^2}{(1 - \beta_p \cos\theta)^2} = 1\,. \tag{A18}$$

We adopt polar angles ψ_{obs} and ϕ_{obs} to describe the apparent orientation of the shock front, so that the components of the unit vector $\hat{\boldsymbol{m}}$ are

$$\begin{aligned} \hat{m}_x &= \frac{m_x}{|m|} = \sin\psi_{\mathrm{obs}} \cos\phi_{\mathrm{obs}}\,, \\ \hat{m}_y &= \frac{m_y}{|m|} = \sin\psi_{\mathrm{obs}} \sin\phi_{\mathrm{obs}}\,, \\ \hat{m}_z &= \frac{m_z}{|m|} = \cos\psi_{\mathrm{obs}}\,, \end{aligned} \tag{A19}$$

where

$$|m| = \left\{\hat{m}_x^2 + \hat{m}_y^2 + \frac{[\hat{m}_z + (\beta_p \sin\theta)\hat{m}_x]^2}{(1 - \beta_p \cos\theta)^2}\right\}^{-1/2} \tag{A20}$$

from equation (A18). Equations (A20) and (A19) can be used to determine the components of the intrinsic shock normal in either the jet (eq. [A17]) or observer (eq. [A15]) reference frame, given the apparent orientation defined by (ψ_{obs}, ϕ_{obs}). The result of this transformation is discussed in § 3 for several line-of-sight angles θ.

When the shock appears exactly edge on ($\psi_{\mathrm{obs}} = 90°$), it is readily shown that the angle between the shock normal and the pattern velocity is given by

$$\cos\psi_{\mathrm{jet}} = (\sin\theta + \beta_a \cos\theta)\frac{\cos\phi_{\mathrm{obs}}}{(1 + \beta_a^2 \cos^2\phi_{\mathrm{obs}})^{1/2}} \tag{A21}$$

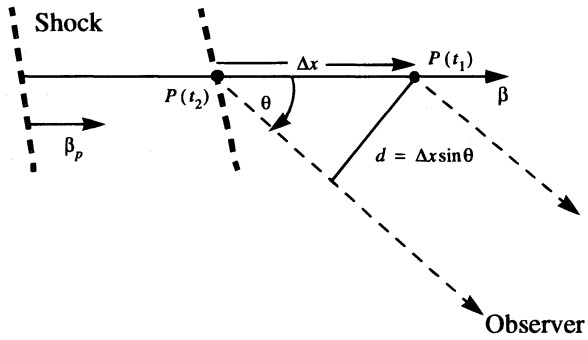

FIG. 18.—This diagram is useful for understanding the relationship between the elapsed proper time of an element of shocked plasma and the size of an aperture placed on a knot. Plasma is shocked at $t = 0$ and by a time t_1 has moved to the edge of the aperture represented by the point $P(t_1)$. In the meantime, the shock, represented by the thick dashed lines, also moves, and $P(t_2)$ is its location at time t_2, given by the condition that rays from $P(t_1)$ and $P(t_2)$ (represented by the thin dashed lines) reach the observer simultaneously. The parameter d is the projected distance between $P(t_2)$ and $P(t_1)$, i.e., the observed aperture.

and that the component of the pattern velocity normal to the shock is

$$\beta_n = \beta_a \frac{\cos \phi_{\rm obs}}{(1 + \beta_a^2 \cos^2 \phi_{\rm obs})^{1/2}} . \tag{A22}$$

The parameter β_n is of particular importance, since it defines the boost of the Lorentz transformation to the shock rest frame. It is remarkable that, in the case of an apparently edge-on shock, this parameter is independent of θ.

A3. THE RELATIONSHIP BETWEEN ELAPSED PROPER TIME OF SHOCKED PLASMA AND APERTURE SIZE

In § 5 we use a relationship for the elapsed proper time of shocked plasma corresponding to a given aperture size. This is derived as follows.

Referring to Figure 18, consider an element of plasma that passes through a shock at $t = 0$ and that subsequently cools, reaching the edge of the fixed aperture, $P(t_1)$, at $t = t_1$. The elapsed proper time is $\gamma^{-1} t_1$, where γ is the postshock Lorentz factor of the plasma. During this time the shock also moves. At a time t_2 it has moved to the location $P(t_2)$ shown on the diagram. The time t_2 is given by the condition that light rays from $P(t_1)$ and $P(t_2)$ reach the observer simultaneously, that is, $t_2 = t_1 - (\Delta x \cos \theta)/c$, where $\Delta x = \beta c t_1 - \beta_p c t_2$ is the separation between the element of plasma and the shock. Thus,

$$\Delta x = (\beta - \beta_p)\gamma c\tau + \beta_p \Delta x \cos \theta , \tag{A23}$$

where τ is the elapsed proper time. Again, referring to the diagram, the aperture size is $d = \Delta x \sin \theta$, so that

$$\tau = \frac{d}{c \sin \theta} \frac{(1 - \beta_p \cos \theta)}{\gamma(\beta - \beta_p)} . \tag{A24}$$

This equation readily shows the differences from the naive estimate of τ resulting from the relative velocity of the shock and plasma, time retardation, and time dilation. This treatment does not take into account the complications resulting from the finite thickness of the postshock flow. However, it should be adequate as an initial estimate of the proper elapsed time.

A4. DESCRIPTION OF OBLIQUE SHOCKS

A4.1. *Relationships among Various Angles*

Several different angles are used to define the geometry of the shocks in the M87 jet: These are the following:

1. The polar angles ($\psi_{\rm jet}$, $\phi_{\rm jet}$) defining the orientation of the shock normal $\boldsymbol{n}$ with respect to the direction of propagation of the shock ($\boldsymbol{k}_{\rm jet}$).
2. The angles θ_1 and θ_2 between the shock normal and the pre- and postshock plasma, respectively, and the deflection angle, $\chi = \theta_2 - \theta_1$.
3. The polar angles (ψ_1, ϕ_1) defining the direction of the preshock plasma with respect to the observer's direction ($\boldsymbol{k}_{\rm obs}$).
4. The polar angles (ψ_2, ϕ_2) defining the direction of the postshock plasma with respect to the observer.
5. The angles $\psi_{1,\rm jet}$ and $\psi_{2,\rm jet}$ defining the directions of the pre- and postshock plasma, respectively, with respect to the shock direction, $\boldsymbol{k}_{\rm jet}$.

Several of these angles are illustrated in Figures 2, 5, and 6. Taking $\boldsymbol{u}_1$ and $\boldsymbol{u}_2$ to be unit vectors in the direction of the pre- and postshock velocity vectors and, as before, $\boldsymbol{n}$ to be the unit normal to the shock, the condition that $\boldsymbol{u}_1$, $\boldsymbol{u}_2$, and $\boldsymbol{n}$ be coplanar implies that

$$\boldsymbol{u}_2 = \frac{\sin \theta_2}{\sin \theta_1} \boldsymbol{u}_1 - \frac{\sin \chi}{\sin \theta_1} \boldsymbol{n} . \tag{A25}$$

The unit vectors $\boldsymbol{u}_1$ and $\boldsymbol{u}_2$ are expressed in terms of the polar angles as follows:

$$\boldsymbol{u}_1 = (\sin\psi_1 \cos\phi_1)\boldsymbol{i}_{\rm obs} + (\sin\psi_1 \sin\phi_1)\boldsymbol{j}_{\rm obs} + (\cos\psi_1)\boldsymbol{k}_{\rm obs}\,, \tag{A26}$$

$$\boldsymbol{u}_2 = (\sin\psi_2 \cos\phi_2)\boldsymbol{i}_{\rm obs} + (\sin\psi_2 \sin\phi_2)\boldsymbol{j}_{\rm obs} + (\cos\psi_2)\boldsymbol{k}_{\rm obs}\,, \tag{A27}$$

where $\boldsymbol{i}_{\rm obs}$, $\boldsymbol{j}_{\rm obs}$, and $\boldsymbol{k}_{\rm obs}$ are the unit vectors along the axes of the observer's frame. The azimuthal angles ϕ_1 and ϕ_2 are determined by the projections of the pre- and postshock velocities onto the sky. For knot A, $\phi \approx \pm 4\overset{\circ}{.}5$ as measured from the jet boundaries. The *projected* deflection of the jet is $\chi_p = \phi_2 - \phi_1$.

The angles θ_1 and θ_2 satisfy

$$\cos\theta_{(1,2)} = \boldsymbol{u}_{(1,2)} \cdot \boldsymbol{n}\,, \tag{A28}$$

where the components of $\boldsymbol{n}$ in the observer's frame are

$$\begin{aligned} n_{x,\rm obs} &= (\cos\theta) n_{x,\rm jet} + (\sin\theta) n_{z,\rm jet}\,, \\ n_{y,\rm obs} &= n_{y\rm jet}\,, \\ n_{z,\rm obs} &= -(\sin\theta) n_{x,\rm jet} + (\cos\theta) n_{z,\rm jet}\,. \end{aligned} \tag{A29}$$

The polar angles (ψ_2, ϕ_2) for the postshock unit vector can be determined from (ψ_1, ϕ_1) via equations (A25) and (A28).

The angles $\psi_{(1,2)\rm jet}$ between the pre- and postshock plasma and the direction of the shock velocity are given by

$$\cos\psi_{(1,2),\rm jet} = \boldsymbol{u}_{(1,2)} \cdot \boldsymbol{k}_{\rm jet} = (\sin\theta) u_{(1,2)x} + (\cos\theta) u_{(1,2)z}\,, \tag{A30}$$

where the components of $\boldsymbol{u}_1$ and $\boldsymbol{u}_2$ refer to the observer's frame and are given by equations (A26) and (A27). One expects these angles to be close to zero.

A4.2. *Shock Junction Conditions*

The shock junction conditions relate downstream (postshock) variables to upstream values. We consider the junction conditions in a frame in which the shock is at rest (the shock frame) and transform between this and the jet frame. There is, in fact, a *family* of shock frames that are all related by Lorentz transformations parallel to the shock front. For the present purpose, the most useful frame is one that is related by a boost of magnitude equal to the normal component, $\beta_n = \beta_p \cos\psi_{\rm jet}$, of the shock pattern speed. The reasons for this choice are as follows. First, since β_n represents the speed of the shock as measured along the normal, the Lorentz transformations between the shock and jet frames are particularly simple, since the normal is selected as the x-axis. Second, as we have seen above, β_n has a special significance in that it and θ are the parameters that specify the relationship between the jet-frame and observed normals (see the derivation of eq. [A14] in § A1). Third, when the observed shock is edge on, β_n is independent of θ (see eq. [A22]). As stated in § 3, taking $(\beta_a, \phi_{\rm obs}) = (0.509, 18^\circ)$ for knot A implies that $\beta_n = 0.44$.

The shock junction conditions in the shock frame (see Fig. 5) are (see, for example, Königl 1980)

$$w_1 \gamma_1^2 \beta_{1\bar{x}} = w_2 \gamma_2^2 \beta_{2\bar{x}}\,, \tag{A31}$$

$$w_1 \gamma_1^2 \beta_{1\bar{x}}^2 + p_1 = w_2 \gamma_2^2 \beta_{2\bar{x}}^2 + p_2\,, \tag{A32}$$

$$w_1 \gamma_1^2 \beta_{1\bar{x}} \beta_{1\bar{y}} = w_2 \gamma_2^2 \beta_{2\bar{x}} \beta_{2\bar{y}}\,, \tag{A33}$$

$$n_1 \gamma_1 \beta_{1\bar{x}} = n_2 \gamma_2 \beta_{2\bar{x}}\,. \tag{A34}$$

Subscripts 1 and 2 denote pre- and postshock plasma, respectively, and we have used bars for the coordinates in order to avoid confusion with the jet and observer coordinates introduced earlier in discussing the orientation of the shock normal. Equations (A31) and (A33) immediately imply that the transverse components of the velocity are equal, i.e., $\beta_{2,\bar{y}} = \beta_{1,\bar{y}}$. (Note that this may not be true if magnetic fields are dynamically important in the shock.) We assume that the plasma pressure is dominated by relativistic matter while an arbitrary amount of cold (subrelativistic) matter contributes to the proper density, implying that the relativistic enthalpy is approximately of the form

$$w = nmc^2 + 4p = \rho c^2 + 4p\,, \tag{A35}$$

where m is the mean mass per cold particle and ρ is the cold matter rest-mass density (very nearly the total rest-mass density). Königl (1980) showed that the ratio $\Delta = \beta_{2\bar{x}}/\beta_{1\bar{x}}$ satisfies the following equation:

$$\left(\frac{u_{1\bar{x}}^2}{\beta_{s1}^2}\right)\Delta^2 - \left(1 + \frac{4}{3}\frac{u_{1\bar{x}}^2}{\beta_{s1}^2}\right)\Delta + \frac{1 + u_{1\bar{x}}^2}{3\beta_{s1}^2} - \left(\frac{1}{3\beta_{s1}^2} - 1\right)[1 + u_{1\bar{x}}^2(1 - \Delta^2)]^{1/2} = 0\,, \tag{A36}$$

where $u_{1\bar{x}} = \gamma_1 \beta_{1\bar{x}}$ is the normal component of the proper preshock velocity and $\beta_{s1} = 3^{-1/2}(1 + \rho c^2/4p)^{-1/2}$ is the sound speed (in units of c). This equation is readily solved for Δ using a Newton-Raphson technique. In the case of a pure relativistic shock ($\beta_{s1,2} = 3^{-1/2}$) the equation for Δ becomes a simple quadratic whose only physical solution gives the well-known result $\beta_{1,\bar{x}} \beta_{2,\bar{x}} = \frac{1}{3}$.

The ratio of post- to preshock pressures is

$$\frac{p_2}{p_1} = \left(\frac{\gamma_1}{\gamma_2}\right)\Delta^{-1}\left[\left(\frac{\gamma_1}{\gamma_2} - 1\right)\mathscr{R}_1 + \frac{\gamma_1}{\gamma_2}\right], \tag{A37}$$

where, as elsewhere in this paper, $\mathscr{R} = \rho c^2/4p$.

To determine the postshock dynamical variables, one selects input values of the preshock Lorentz factor γ_1 and angle θ_1 in the jet frame and calculates the corresponding values in the shock frame, using

$$\beta_{1\bar{x}} = \frac{\beta_1 \cos\theta_1 - \beta_n}{1 - (\beta_1 \cos\theta_1)\beta_n}, \tag{A38}$$

$$\beta_{1\bar{y}} = \frac{\beta_1 \sin\theta_1}{\gamma_n[1 - (\beta_1 \cos\theta_1)\beta_n]}. \tag{A39}$$

Postshock values of velocity and pressure, etc., are calculated in the shock frame using equation (A36) above, and the postshock variables are transformed back to the jet frame via the inverse Lorentz transformation. As the angle θ_1 increases, eventually $p_2/p_1 = 1$, defining the Mach angle *in the jet frame.*

REFERENCES

Begelman, M. C. 1996, in Cygnus A: Study of a Radio Galaxy, ed. C. L. Carilli & D. E. Harris (Cambridge: Cambridge Univ. Press), 209
Bicknell, G. V., Dopita, M. A., & O'Dea, C. P. 1996a, in preparation
———. 1996b, in IAU Symp. 175, Extragalactic Radio Sources, ed. R. D. Ekers, C. Fanti, & L. Padrielli (Dordrecht: Kluwer), in press
Binette, L., Dopita, M. A., & Tuohy, I. R. 1985, ApJ, 297, 476
Binney, J., & Tabor, G. 1995, MNRAS, 276, 663
Biretta, J. A. 1993, in STScI Symp. 6, Astrophysical Jets, ed. D. Burgarella, M. Livio, & C. P. O'Dea, (Cambridge: Cambridge Univ. Press), 263
Biretta, J. A., & Meisenheimer, K. 1993, in Lecture Notes in Physics, Vol. 421, Jets in Extragalactic Radio Sources, ed. H. J. Röser & K. Meisenheimer (Berlin: Springer), 159
Biretta, J. A., Stern, C. P., & Harris, D. E. 1991, AJ, 101, 1632
Biretta, J. A., Zhou, F., & Owen, F. N. 1995, ApJ, 447, 582
Birkinshaw, M. 1984, MNRAS, 208, 887
Böhringer, H., Nulsen, P. E. J., Braun, R., & Fabian, A. C. 1995, MNRAS, 274, L67
Bolton, J. G., Stanley, J. G., & Slee, O. B. 1949, Nature, 164, 101
Coleman, C. S., & Bicknell, G. V. 1988, MNRAS, 230, 497
Conway, J. E., Myers, S. T., Pearson, T. J., Readhead, A. C. S., Unwin, S. C., & Xu, W. 1994, ApJ, 425, 568
Curtis, H. D. 1918, Pub. Lick Obs., 13, 31
Dopita, M. A., & Sutherland, R. S. 1996a, ApJS, 102, 161
———. 1996b, ApJ, 455, 468
Ford, H. C., & Butcher, H. 1979, ApJS, 41, 147
Ford, H. C., et al. 1994, ApJ, 435, L27
Freedman, W. L., et al. 1994, Nature, 371, 757
Hardee, P. E. 1982, ApJ, 261, 457
———. 1987a, ApJ, 313, 607
———. 1987b, ApJ, 318, 78
Hines, D. C., Owen, F. N., & Eilek, J. A. 1989, ApJ, 347, 713
Klein, R. I., McKee, C. F., & Colella, P. 1994, ApJ, 420, 213
Königl, A. 1980, Phys. Fluids, 23, 1083
Komissarov, S. S. 1994, MNRAS, 269, 394
Landau, L. D., & Lifshitz, E. M. 1987, Fluid Mechanics (2d English ed.; Oxford: Pergamon)
Marscher, A. P., Gear, W. K., & Travis, J. P. 1991, in Variability of Blazars, ed. E. Valtaoja & M. Valtonen (Cambridge: Cambridge Univ. Press), 85
Meisenheimer, K., Röser, H.-J., & Schlötelburg, M. 1996, A&A, 307, 61
Norman, M. L., Winkler, K.-H., & Smarr, L. L. 1984, in Physics of Energy Transport in Extragalactic Radio Sources, ed. A. H. Bridle & J. A. Eilek (Green Bank: NRAO), 150
Owen, F. N., Eilek, J. A., & Keel, W. C. 1990, ApJ, 362, 449
Owen, F. N., Hardee, P. E., & Bignell, R. C. 1980, ApJ, 239, L11
Owen, F. N., Hardee, P. E., & Cornwell, T. J. 1989, ApJ, 340, 698
Padovani, P., & Urry, C. M. 1990, ApJ, 368, 373
Phinney, E. S. 1983, Ph.D. thesis, Univ. Cambridge
Rees, M. J. 1966, Nature, 211, 468
Sargent, W. L. W., Young, P. J., Boksenberg, A., Shortridge, K., Lynds, C. R., & Hartwick, F. D. A. 1978, ApJ, 221, 731
Sparks, W. B., Ford, H. C., & Kinney, A. L. 1993, ApJ, 413, 531
Sparks, W. B., Fraix-Burnet, D., Machetto, F., & Owen, F. N. 1992, Nature, 355, 804
Sutherland, R. S., Bicknell, G. V., & Dopita, M. A. 1993, ApJ, 414, 510
Sutherland, R. S., & Dopita, M. A. 1993, ApJS, 88, 253
Turland, B. D. 1975, MNRAS, 170, 281
Weaver, R., McCray, R., Castor, J., Shapiro, P., & Moore, R. 1977, ApJ, 218, 377
White, R. E., & Sarazin, C. L. 1988, ApJ, 335, 688
Wilkinson, P. N., Polatidis, A. G., Readhead, A. C. S., Xu, W., & Pearson, T. J. 1994, ApJ, 432, L87